Summer 2022

Quasi-Static Structural Analysis of an Experimental Aircraft Wing

Scott Bender
Embry-Riddle Aeronautical University, benders3@my.erau.edu

QUASI-STATIC STRUCTURAL ANALYSIS OF AN EXPERIMENTAL AIRCRAFT WING

By

Scott Bender

A Thesis Submitted to the Faculty of Embry-Riddle Aeronautical University

In Partial Fulfillment of the Requirements for the Degree of

Master of Science in Aerospace Engineering

August 2022

Embry-Riddle Aeronautical University

Daytona Beach, Florida

QUASI-STATIC STRUCTURAL ANALYSIS OF AN EXPERIMENTAL AIRCRAFT WING

By

Scott Bender

This Thesis was prepared under the direction of the candidate's Thesis Committee Chair, Dr. Daewon Kim, Department of Aerospace Engineering, and has been approved by the members of the Thesis Committee. It was submitted to the Office of the Senior Vice President for Academic Affairs and Provost, and was accepted in the partial fulfillment of the requirements for the Degree of Master of Science in Aerospace Engineering.

THESIS COMMITTEE

Chair, Dr. Daewon Kim	Member, Dr. Alberto Mello
Member, Dr. Jeff Brown	Member, Professor Joe Martin
Graduate Program Coordinator, Dr. Hever Moncayo	Date
Dean of the College of Engineering, Dr. James W. Gregory	Date
Associate Provost of Academic Support, Dr. Christopher Grant	Date

In Memory of Michael Horwitz.

ACKNOWLEDGEMENTS

Often we traverse life in search of meaning or purpose. While we may end up in a place we'd never expect, those who support our journey through light and dark are the reason we keep searching. Thank you to my mother, family, and friends who have belived in me since the start. Thank you to the teachers and mentors that have molded my mind to think critically about the world around me. Thank you to my advisor, Professor Daewon Kim, who has given me guidance when I needed it most. Thank you to Professor Joe Martin for his dedication to this project along with his vast knowledge and experience. Thank you to Bill Russo who has taught me how to mold imagination into reality. Thank you to Mike Potash for his expertise in electrical engineering and for developing the quartermaster many years ago. And thank you to you, the reader, I hope my experiences will guide you shall you ever find yourself in need.

ABSTRACT

In this report, a quasi-static load analysis is conducted on an experimental light sport aircraft wing via a whiffletree bending test. This report will discuss the loads present on the aircraft during straight level flight at a speed of 82 knots equivalent air speed. Flight load calculations are described along with the design of the whiffletree and mounting structures utilized for applying the distributed point loads. Initial finite element analysis is performed on the wing structure to determine critical strain locations and optimal sensor distribution. Subsequent mechanical experimentations are performed using a bending test to measure the strain at critical locations along the wing structure using resistive uniaxial strain gauges. To verify the applied load distribution is accurate, the load on the critical connecting rod is evaluated during experimentation. The accuracy of the finite element method is compared to the data calculated using the strain gauges. Additionally, the displacement of the wing structure is compared to that of the finite element model. Recommendations for future experimentation to improve the model and whiffletree structure are discussed. From the results, it is evident that an accurate representation of the distributed flight load was applied to the wing structure test article. Utilizing the three data sets collected, the standard deviation in the strain gauge data was analyzed to identify potential outliers that indicate sensor malfunction. Comparing the experimental and finite element results, it is clear that both models are sufficient in accurately representing the strain distribution about the forward spar and front stringer but vary in strain measurements along the aft spar. This variation is likely due to oversimplifications in the finite element model.

TABLE OF CONTENTS

LIST OF FIGURES

LIST OF TABLES

NOMENCLATURE

G	Acceleration of gravity
c	Chord length
V_∞	Freestream velocity
α	Angle of attack
$\alpha_{L=0}$	Zero lift angle of attack
T_p	Tensile load on each machine screw
b'	Distance between side of angle beam and edge of the loading hole
P	Width of angle bracket
F_y	Tensile yield stress
SWB	Spanwise Beam
CWB	Chordwise Beam
b	Base Length
h	Height
A	Cross-sectional area for each section
A_{total}	Area of entire cross section
$\bar{y}$	Distance from the reference axis to the center of each segment
Y	Distance from the reference axis to the neutral axis
I_{NA}	Moment of Inertia about the neutral axis for each segment
$I_{x,ref.}$	Moment of Inertia about the reference axis
$I_{x,NA.}$	Moment of Inertia about the neutral axis
y_t	Distance from the neutral axis to the point of highest tension in bending
y_c	Distance from the neutral axis to the point of highest compression in bending

M.S.	Margin of safety
I_x	Moment of Inertia acting about the x-axis
M_x	Moment acting about the x-axis
$f_{b,t}$	Tensile bending stress
$f_{b,c}$	Compressive bending stress
F_{tu}	Ultimate tensile stress
F_{cy}	Compressive yield stress
K_{tgB}	Hole stress concentration factor
M_{max}	Maximum moment
H	Height of beam
t	Thickness of beam
$\sigma_{max,B}$	Hole concentration stress
f_s	Hole tear-out stress
x’	Distance between edge of hole and edge of beam
P	Normal force
f_{br}	Bearing stress
σ_t	Tensile stress
τ_{avg}	Average shear stress
K	Width of angle bracket
T_p	Load on one bolt
F_{ty}	Tensile yield stress
t_{req}	Required thickness
t_{actual}	Actual thickness

k_t	Tensile efficiency factor
k_{br}	Shear-bearing efficiency factor
F_{bru}	Ultimate bearing stress
P_{br}	Bearing load

1 Introduction

During routine flight Aircraft undergo substantial repetitive loading that has a significant effect on the lifecycle of the overall structure. Particularly, this repetitive loading is often experienced in the form of wing deformation with maximum loads experienced while performing maneuvers at a designed maneuvering velocity. As such, in part 25 of the Federal Aviation Regulation airworthiness standards, aircraft wings are required to undergo static ultimate load testing for a minimum of 3 seconds using loads that closely represent the actual conditions experienced by the aircraft during flight. Such testing is also required to meet the requirement of the ASTM F2245-16c standards for the design of light sport aircraft. Typically, the ultimate load that must be applied is determined by multiplying the limit load by the prescribed factor of safety for the aircraft.

As the described research is not intended to verify the flight requirements for the examined wing, tests will only be conducted to a force equivalent to straight level flight of 1G completed at maneuvering velocity. Such loading is measured such that the loaded wing does not experience any plastic deformation, as the load will remail below the limit load, and can be utilized for future load testing.

As a result, this paper will focus on the quasi-static load analysis and finite element analysis of a light sport aircraft wing with a load distribution equivalent to that of a 1G pull-up-maneuver at maneuvering velocity. In addition, this paper will discuss the detailed design and development of the whiffletree structure used to apply the calculated static flight load distribution. Moreover, the results of the finite element simulation, experimental testing using strain gauges, and wing deflection will be discussed.

1.1 Background

The verification of theoretical stress in aircraft wing structures is crucial to ensure the safety of the Aircraft's operators and passengers. As such, aircraft wing stress analysis utilizing wing

bending tests has been a staple in aircraft safety analysis since the early 1900s. Early tests were typically performed by inverting the wing structure and applying a distributed load on the bottom of the wing using sandbags that approximate the actual loads experienced by the aircraft, as shown in Figure 1.1.

Figure 1.1 Static Testing of a Monoplane Wing using Sandbags in 1911 [1].

Testing aircraft using the described sandbag method is still an acceptable method for applying an accurate load distribution on aircraft wing to verify theoretical finite element analysis models [2–4]. As methods of finite analysis improved, more advanced techniques for model verification were also independently improved [5]. One of those methods, a Whiffletree bending test, will be described in detail in this paper. For such test, an initial load, typically provided by one or multiple

hydraulics, is spread along the entire wing structure using spreader beams, as demonstrated in Figure 1.2. Utilizing a whiffletree structure not only allows for a comparable load distribution, but also allows for the facile adjustment of lifting loads to test for maneuvers at different G-forces to verify the structural integrity of the aircraft wing.

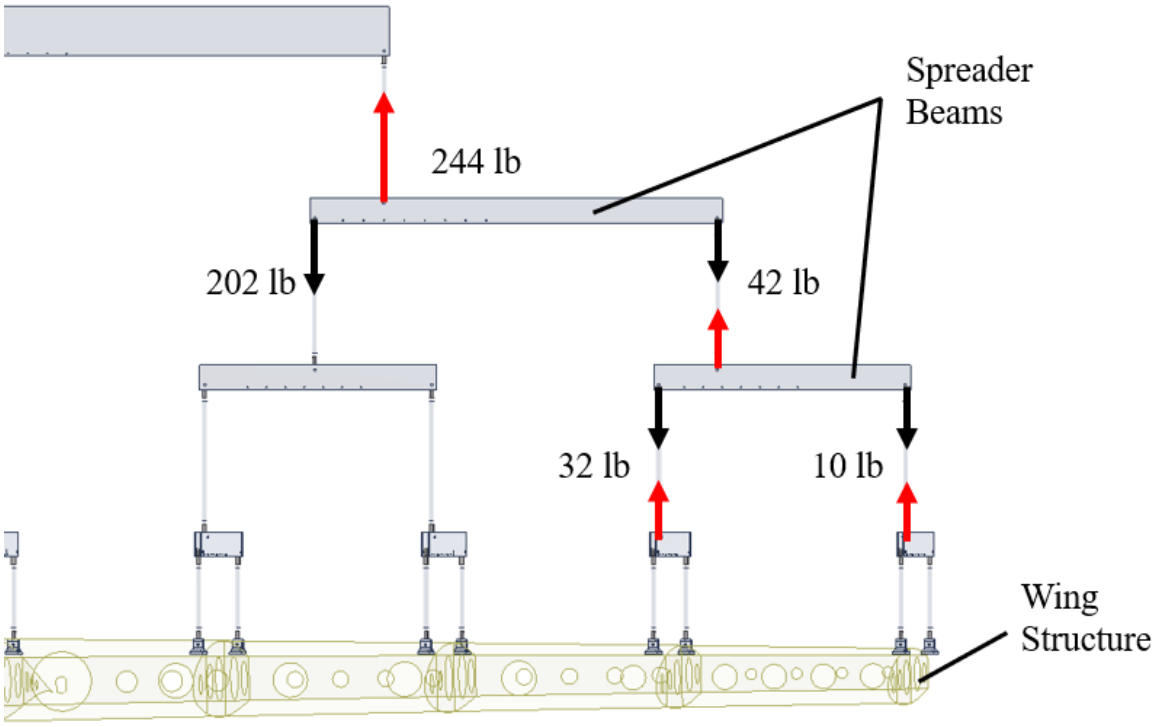

Figure 1.2 Whiffletree Spreader Beams and Wing Structure

As this paper is merely concerned with establishing a verifiable technique for load analysis of an aircraft wing at Embry-Riddle Aeronautical University, a previously developed light sport aircraft wing model was utilized for analysis. A picture of the aircraft is shown in Figure 1.3. The light sport aircraft wing analyzed was previously constructed, analyzed, and flight tested by Joe Martin, a professor of aerospace engineering at Embry-Riddle Aeronautical University. The flight test performed can best be described as series a high-speed taxi runs in which the aircraft was

briefly airborne to test control authority. While the developed experimental aircraft received experimental airworthiness certification and was loaded to 2.5G using a sandbag test, it was not certified by the Federal Aviation Administration due to financial difficulties by the company responsible for the aircraft's development.

Figure 1.3 Experimental Light Sport Aircraft [6].

Moreover, this report will utilize a basis that was set forth by previous students at Embry-Riddle Aeronautical University to establish a method of performing mechanical analysis on a light sport aircraft wing. A modified design process will be presented that provides details not considered by those who previously contributed to the completion of this project.

1.2 Motivation and Scope of Thesis

This work examines the stress distribution experienced by a light sport aircraft wing structure during level flight using finite element modeling and discusses the development and analysis of the whiffletree testing structure used to mechanically verify the theortical analysis. The overall goal of the described research is to provide, for the first time at Embry-Riddle Aeronautical

University, a detailed method of developing a whiffle tree structure for the verification of the stress experienced by a previously tested light sport aircraft wing structure under calculated flight loads. In addition, a finite element model will also be established and a relative comparsion made using data obtained from strain gauges adhered along the spanwise and chordwise distribution of the tested aircraft wing.

For the establishment of the theoretical load distribution experienced by the aircraft wing, Anderson's method was introduced [7]. Such a method is an acceptble determination of lift distribution that establishes a basis for wing loading utilizing the aircraft wings geometric features. Additionally, the conversion of the calculated aerodyamic flight loads to point loads will be discussed, thus, leading to the design and analysis of the whiffletree structure that was utilized during experimentation to apply quasi-static flight loads up to 1G.

While this report will include into the theoretical development of a whiffletree structure, the overall goal is to provide Embry-Riddle Aeronautical University with a verifiable whiffletree structure that can be utilized in future experimentation. Additionally, this report aims to provide students at Embry-Riddle Aeronautical University an opportunity to learn how to effectivly perform quasi-static flight load analysis using a whiffletree structure. Such experimentation will improve the experimental facilities at Embry-Riddle Aeronautical University's department of engineering and provide a basis for addition learning about how previously developed aircraft structures are verified for flight. Such basis will be established by providing students with the opportunity to compare the finite element models they develop with the experimental strain gage results presented in this report.

2 Review of the Relevant Literature

This section will review relevant literature pertaining to the theoretical loads experienced by aircraft wings during flight. Additionally, previous experimentation focused on quasi-static load testing will be discussed in detail. Considering such experimentation, equipment and technology utilized to measure loads on aircraft wings, particularly strain and deflection, will be discussed.

2.1 Loads on Aircraft Wings

During flight aircraft wings undergo several types of loading that must be considered when evaluating the aircraft flight performance. As aircraft wings are the primary source of lift for an aircraft, it is important that theoretical calculations accurately reflect the actual wing model [8]. The primary load acting on the aircraft wing is the aerodynamic load involving both forces, lift and drag, and moments, bending and wing torsion. Additionally, local lift values are highly dependent on the geometry of the wing rather than dynamic pressure, load factor, and weight [9]. Considering such, the spanwise lift distribution can be utilized as an accurate method for predicting structural loads acting on the wings surface [10]. Thus, low-cost computational methods of determining the wing lift distribution were explored including Prandtl's Lifting Line Theory and Anderson's method.

Prandtl's lifting line theory is widely considered as the first practical theory utilized for calculating the aerodynamic properties for a finite wing. Prandtl's theory is largely based on assumptions of potential flow that the physical flow around an object can be represented by vortices distributed along a freestream [11–13]. In addition to the vortices a bound vortex filament is assumed along the aerodynamic center of the wing with two free vortices trailing from both ends of the wing as to satisfy Helmholtz's theorem that a vortex filament cannot end in a fluid [12]. The combination of such vortices can be denoted as a horseshoe vortex. To accurately represent the lift

distribution, an infinite number of horseshoe vortices are superimposed along the aerodynamic center.

For a finite wing with a given freestream geometric angle of attack and airspeed velocity, the aerodynamic quantities for α, c, V_∞, and $\alpha_{L=0}$ are known. These values are utilized in tandem with the Kutta-Joukowski theorem to determine the aerodynamic characteristics of the aircraft wing surface, namely the coefficient of lift which can be implemented to determine the loading present on the wing during flight. While the Prandtl lifting line theory is excellent at predicting the aerodynamic characteristics of straight wings with moderate to high aspect ratios, such method is not accurate for low-aspect-ratio straight wings, delta wings, or swept wings. As the wing ultimately utilized in this report is swept, it is evident that an alternative method of determining aerodynamic wing characteristics must be explored.

Anderson's method is an alternative method regarded as a highly reputable technique for determining the aerodynamic characteristics on aircraft wing surfaces. The goal of such method was to improve on previous methods of determining the theoretical aircraft wing characteristics including span lift distribution, induced-angle of attack distribution, angle of zero lift, aerodynamic-center position, induced drag, and the pitching moment about the aerodynamic center. Furthermore, Anderson's method provided a theoretical approach that could be applied to wings with a large range of aspect ratios and taper ratios in addition to wings that have twist and sweepback [7].

The basis of Anderson's work is accredited to Glauert who introduced Fourier series as a method for adapting linear lift curves to wings of any twist or plan form [7,14]. As such, Anderson's method considers the spanwise lift distribution on an aircraft wing to be constructed of two parts, the basic distribution, depending principally on the twist of the when total lift is zero,

and the additional distribution, the change of lift due to the angle of attack of the wing [7]. The results of Anderson's work are presented in tables and charts that can be easily applied to determine the lift characteristics of wings with a wide range of taper ratios and aspect ratios ranging from 2 to 20. Additionally, the effects of sweepback and twist are considered and such theoretical calculations can be easily applied to straight taper plan forms such as the experimental aircraft examined in this report [7]. Due to the simplicity and high accuracy of Anderson's method for the intended purpose of the aforementioned experimental light sport aircraft, such method was adapted for determining the aerodynamic characteristics utilized in this report.

2.2 Aircraft Wing Quasi-Static Load Testing

The analysis and application of quasi-static theoretical flight load testing is a widely applied method in the aerospace industry for verifying the mechanical integrity of aircraft components, particularly wing structures [5,15–17]. In regard to wing structures, the overall goal of such testing is to examine the wing's ability to resist bending and torsional loads and moments that the wing will experience during flight. As such, researchers and aircraft designers have developed advanced methods of applying quasi-static flight loads to structures and measuring the structure's strain and deformation.

Considering the advancement and availability of high strength hydraulic technology, one of the more reliable techniques for distributing load is through a system of hydraulic cylinders. By adhering hydraulic cylinders to load pads using load cells, one can finely adjust the applied load on the lower and upper surfaces of the wing. Such a method allows for a highly accurate applied flight distribution, since loads can be applied to not only the ribs, as well as the ability to finely adjust loading patterns to replicate that of actual flight. In some cases, string potentiometers can be suspended above and adhered to the surface of a wing to get an accurate deformation measurement during experimentation [16].

Another common method for analyzing aircraft wings in bending due to aerodynamic loading is through a whiffletree configuration. Such configuration allows for a spanwise and chordwise distribution to be designed in a tree-like structure. Whiffletrees are extremely popular for applying loads to wings due to their ability to effectively distribute the flight load at various conditions [18,19]. While whiffletrees do not have the same flexibility with load distribution as a series of hydraulic pads, they are much more cost effective. Additionally, the whiffletree load can be applied from above with the wing oriented in its normal operational position, or in a hanging instance by inverting the wing structure [20]. Loading for whiffletrees is typically applied using one or multiple hydraulic cylinders or by applying weights to the wing structure [21].

Adhering whiffletree to the ribs of the wing to apply the designed load is typically achieved by developing saddles or external wood sleeves that encases the rib structure [22]. Such method allows for the distribution of load to be applied along the entire rib structure, preventing failure that may occur using single point connections. An alternative method of adhering loading points on the aircraft wing to the whiffletree is through utilizing pads that are bonded to the surface of the wing [21]. While this method may lead to single point failure, it provides a cost benefit as it reduces the material required and eliminates the complexity of developing a saddle structure.

A third method utilized for applying quasi-static flight loads to a wing structure is through the use for sandbags [19]. Sandbag loading is typically done by inverting the aircraft wing and placing sandbags on the underside of the wing. While such loading is an effective method of modeling the actual pressure distribution present on the wing surface, applying large loads can be inherently dangerous as failure of the wing could result in sandbags falling onto technicians applying the sandbags to the structure. Additionally, it is difficult to adjust the loading on the wing so testing different loading forces is difficult and will cost a significant amount of time and labor. Aside from

the risks associated with large loads, sandbag loading is the most affordable method of loading in comparison to the hydraulic cylinders and whiffletree loading methods.

In conclusion, this report will utilize a whiffletree as the primary method of loading as the multiple hydraulic pad system is too expensive and the sandbag method is unideal for quickly testing different load cases. Considering the different methods of mounting the whiffletree to the wing structure, using point load pad attachments is considered most time efficient and cost effective and thus, will be integrated into the development of the wing loading structure.

2.3 Strain Measurement devices

This section will evaluate different methods of measuring strain experienced by aircraft wings while encountering flight loads. Partially, this section will evaluate conventional methods in aircraft structural load testing for measuring strain including strain gauges, fiber optic sensing systems, and digital image correlation. Such sensors provide unique methods of measuring strain that can be utilized to determine the stress and displacement experienced by the aircraft wing while undergoing loading.

Strain gauges are considered the gold standard for measuring strain on components subject to loading. In the aerospace industry, strain gauges have a reputation for high fidelity strain measurements and are considered the standard while performing any load analysis [16]. Strain gauges operate by establishing a relationship between resistance change with length. As such, when a strain gauge is properly adhered to a surface that experiences strain, the resistance of the strain gauge changes and is measured as a voltage change using a digital acquisition system. As aircraft wing is tested in the elastic regime, a relationship between the measured strain on the aircraft wing can be translated to a stress that can be compared to theoretical results.

Another promising technology for measuring strain on aircraft wing is a fiber optic sensing system. With recent advancements in high-definition fiber optic sensing, fiber optic sensing

systems have become more promising for measuring strain and displacement as fiber Bragg grating is no longer required. High-definition fiber optics operate by utilizing Rayleigh backscatter to detect changes in strain relative to the optical fingerprint of the fiber optic wire [23]. Such technology allows for the continuous monitoring of strain along the wing surface. While impressive, this innovative technology is expensive compared to the aforementioned strain gauges.

Digital image correlation has also shown promise as a method of measuring strain on the surface of wings during quasi-static load analysis [24]. Digital image correlation operates by using a high-definition camera to detect changes in the movement of particles or dots on the test structure and measure the displacement field. This displacement field can then be utilized to calculate strain or indicate buckling [25]. While digital image correlation presents a unique method of measuring strain of an object, equipment with resolution required to analyze the strain and displacement distribution along the aircraft wing is expensive.

Considering the availability, cost, and accuracy of the different sensor types mentioned, it is evident that strain gauges yield the highest accuracy while maintaining a relatively low cost. As such, strain gauges were chosen as the primary form of mechanical strain measurement. While fiber optic and digital image systems were not demonstrated in the presented work, it is evident that these sensing systems are promising technology that can be adapted to the experimental aircraft wing model in future experimentation.

2.4 Summary

After reviewing literature on the loads acting on the aircraft wing, it is evident that Anderson's method is most ideal for representing the spanwise aerodynamic flight loads acting on the structure. While such method of aerodynamic analysis is simple in nature, it provides accurate results that will be utilized during experimentation.

In regard to the loading method, a whiffletree structure is deemed the most cost and time efficient method to apply the determined aerodynamic flight loads onto the wing structure. As whiffletree structures can easily vary load applied to the aircraft wing, such structure is ideal for the experimentation that will be detailed in this report.

Additionally, for measuring the strain that will be experienced by the aircraft structure, it is evident that foil strain gauges provide both the accuracy and cost effectiveness required for the described experimentation. Particularly, as the experimental loading discussed in this report is only aimed at measuring bending along the span of the aircraft wing, uniaxial foil strain gauges are ideal.

2.5 Hypothesis

The expected result of such experimentation is to provide a reliable testing model for measuring the strain and stress on the surface of an experimental aircraft wing. Additionally, this report will utilize the known geometry of the experimental light sport aircraft wing being analyzed to produce a high-fidelity finite element analysis model. The developed model will be validated using the experimental results obtained through strain gage testing. Additionally, the displacement at the tip of the wing will be measured and compared to the finite element model to establish a connection between the theoretical model and actual deformation under load. A computer generated model of the test structure that will be developed in this report is presented in Figure 2.1.

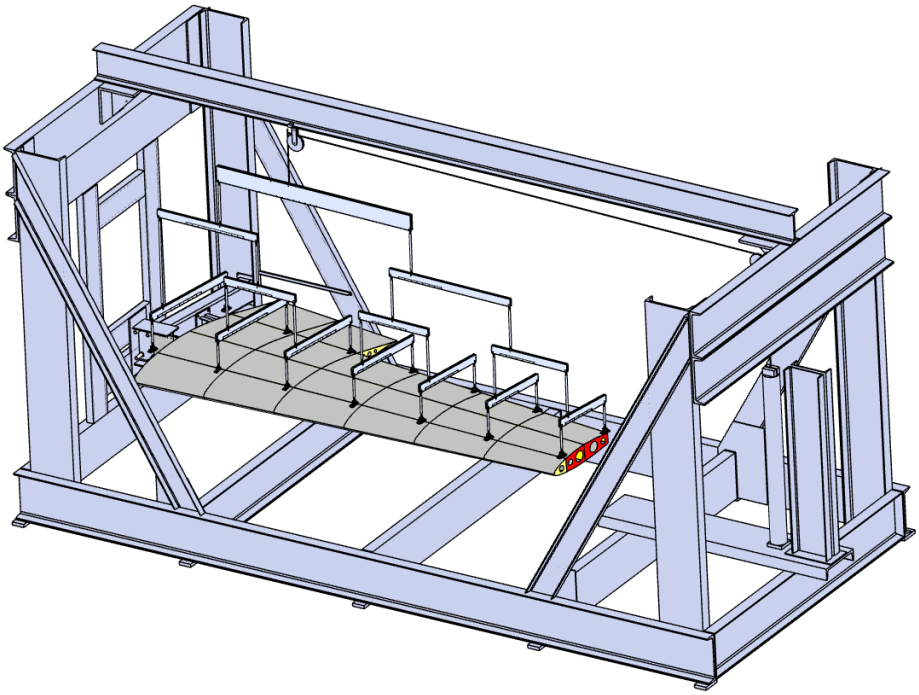

Figure 2.1 Developed Experimental Testing Apparatus.

3 Experimental Approach

This section will describe the experimental approach that was taken to develop the whiffletree structure and perform the quasi-static load testing of the wing. Such approach will include the development of the whiffletree structure including the theoretical stress calculations to ensure the structure is safe for operation. In addition, the materials and equipment used during development of the testing structure will be described. Finally, the experimental procedures followed for adhering sensors to the wing structure and the analysis of such sensors will also be discussed.

3.1 Development of the Whiffletree Structure

In this section the theoretical aerodynamic load distribution and pointwise load distribution will be examined. Moreover, the development and mechanical analysis of the whiffletree structure that was used to apply the theoretical quasi-static flight load onto the experimental aircraft wing structure will be discussed. As such, a detailed breakdown of each section of the whiffletree will be described including the spreader beams, connecting rods, and connection pads. Additionally, this section will describe the process and methods utilized during the fabrication of the whiffletree structure.

3.1.1 Theoretical Aerodynamic and Point Load Distribution

This report will include previous calculations executed by Professor Joe Martin and his team while prototyping the light sport aircraft. As such, to determine the flight loads experienced by the aircraft wing, theoretical analysis was complete using Anderson's method. Such method integrates the designed wing geometry with data previously obtained through experimentation to estimate flight loads experienced by aircraft wing geometry. As detailing the calculations for Anderson's method is not within the scope of this report, these calculations will not be addressed directly but the derivation of Anderson's method is readily available [7]. The geometry utilized with

Anderson's method to determine the flight load distribution is shown in Figure 3.1 and the calculated lift distribution is presented in Figure 3.2.

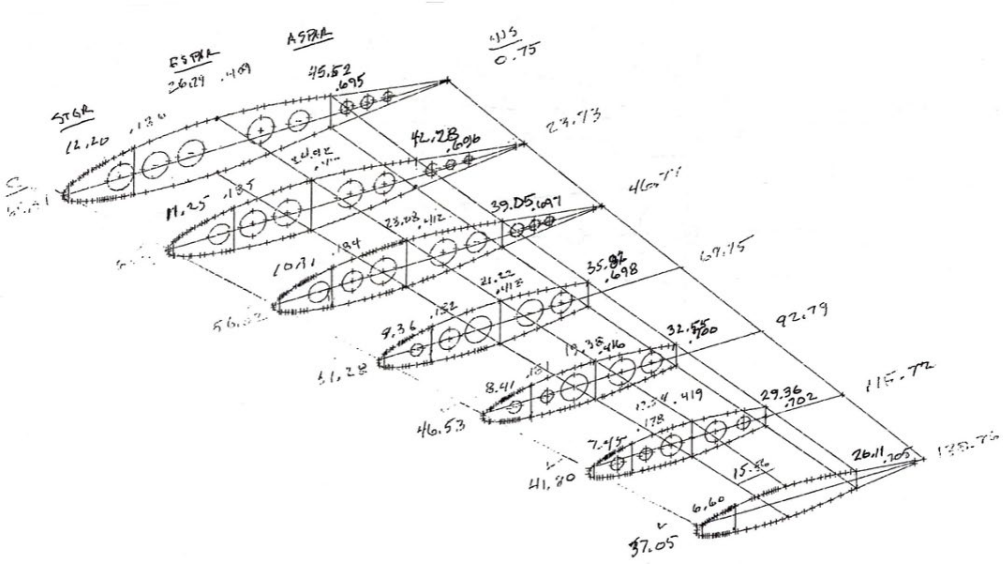

Figure 3.1 Experimental Aircraft Wing Drawing [26].

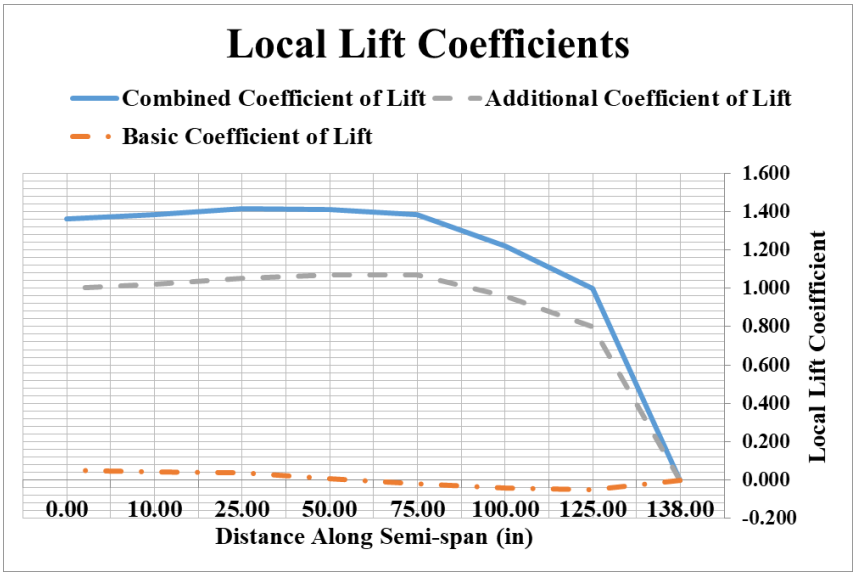

Figure 3.2 Aircraft Lift Coefficients Using Anderson's Method [26].

Utilizing the flight load distribution calculated using Anderson's Method, the concentrated force acting on each rib was determined. This rib-wise distribution along with the location of the ribs relative to the root is presented in Table 3.1. To distribute the load across the entire chord of the aircraft wing, the two connection points were chosen to be the front stringer and the rear spar. The spanwise load is distributed along the aerodynamic center of lift designed at 26 percent of the chord length. As such, the distance between the aerodynamic center of lift and the front stringer and aft spar were utilized to establish the load that will be acting on the wing connection points. These resultant loads are shown in Table 3.2.

Table 3.1 Rib locations and normal force loading.

Ribs	**Location from Root (in)**	**Fz (lbf)**
Rib 1	0	154
Rib 2	22.5	139
Rib 3	46	123
Rib 4	69	104
Rib 5	92	98
Rib 6	115	32
Rib 7	154.72	10

Table 3.2 Normal loads acting on the front stringer and aft spar.

Ribs	Front Stringer Load (lbf)	Aft Spar Load (lbf)
Rib 1	132	22
Rib 2	119	20
Rib 3	105	18
Rib 4	88	16
Rib 5	83	15
Rib 6	27	5
Rib 7	8	2

The calculated spanwise and chordwise distribution will provide basis for the development of the whiffletree assembly structure highlighted in the following section.

3.1.2 Analysis and Assembly of Whiffletree Spreader Beams

Utilizing the spanwise load previously calculated using Anderson's method, the whiffletree was designed using the theoretical sum of loads for a simply supported beam to determine the approximated loading for each rib. To determine the location of the center hole the known forces, Az and Bz, are used in junction with the known distance, the sum of A and B. The location of the center hole for each beam is indicated by Fz in the free body diagram shown in Figure 3.3**.** For the spanwise spreader beams positioned along the top of the chordwise beams, the known distance is the length between the ribs.

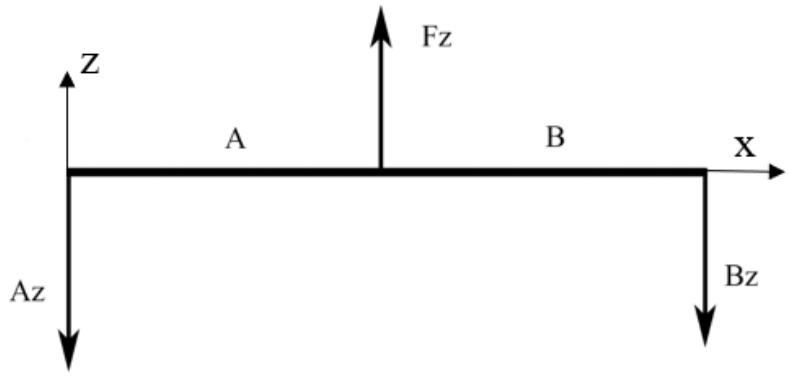

Figure 3.3 Theoretical Force Distribution for a Simply Supported Beam.

From such loading, we can determine the theoretical equations for calculating the distances A and B relative to the designed load distribution utilizing sum of loads to establish the location of the center hole. The equation utilizing the static assumption that the sum of loads in the z-direction are zero yields equation 3.1.

$$A_z + B_z = F_z \tag{3.1}$$

To determine the lengths of A and B, the theoretical assumption that the sum of moments caused by the forces in the z-direction is zero is used. The moment diagram for the simply supported structure is presented in Figure 3.4**.**

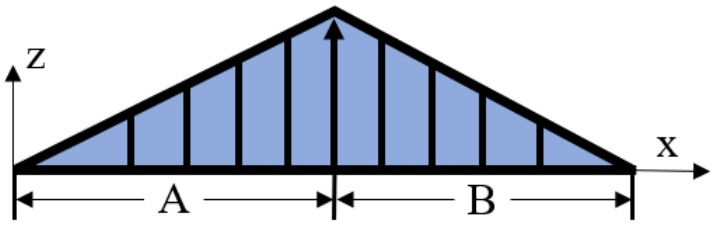

Figure 3.4 Theoretical Moment Distribution for a Simply Supported Beam.

As such, considering the loading and moment distribution, the resultant equation from the sum of moments is presented below:

$$B_z = \frac{F_z \times A}{A + B} \tag{3.2}$$

Considering the chordwise beams, the length of A and B were determined by the distances between the connection points at the front stringer and rear spar from the aerodynamic center of lift. The dimensions for A, the distance between the aerodynamic center to the front stringer, and B, the distance between the rear spar and the aerodynamic center, for each chordwise beam is presented in Table 3.3.

Table 3.3 Chordwise beam end hole locations relative to the center hole.

Beam	**Location**	**A (in)**	**B (in)**
CWB1	Rib 1	4.83	28.49
CWB2	Rib 2	4.55	26.48
CWB3	Rib 3	4.26	24.48
CWB4	Rib 4	3.97	22.49
CWB5	Rib 5	3.69	20.45
CWB6	Rib 6	3.42	18.49
CWB7	Rib 7	3.03	16.48

From the initial hole location for the chordwise beams located along the aerodynamic center, the distance between the spanwise beams connecting to the chordwise beams is known. Utilizing this initial distance and the theoretical load and moment equations, the required distances to distribute the spanwise load was determined. These distances are presented in Table 3.4.

Table 3.4 Spanwise beam end hole locations relative to the center hole.

Beam	**A (in)**	**B (in)**
SWB1	41.64	24.42
SWB2	12.41	21.12
SWB3	33.77	7.02
SWB4	12.47	11.03
SWB5	11.84	11.16
SWB6	19.05	5.95

After calculating the required distances for distributing the designed load, the theoretical max bending moment for simply supported beams can be implemented to determine the max bending load and thus, the beam dimensions required to resist such bending. The equation for the max bending moment for simply supported beams is presented below:

$$M_{max} = \frac{F_z \times A \times B}{A + B} \tag{3.3}$$

As both the spanwise and chordwise spreader beams were designed using a two-beam design, shown in Figure 3.5, in which both beams were constructed with Al 6061-T6511 and held together by high strength steel bolts, it is evident that each beam only experiences half of the designed load. As such, each beam was separately designed and analyzed to resist longitudinal bending.

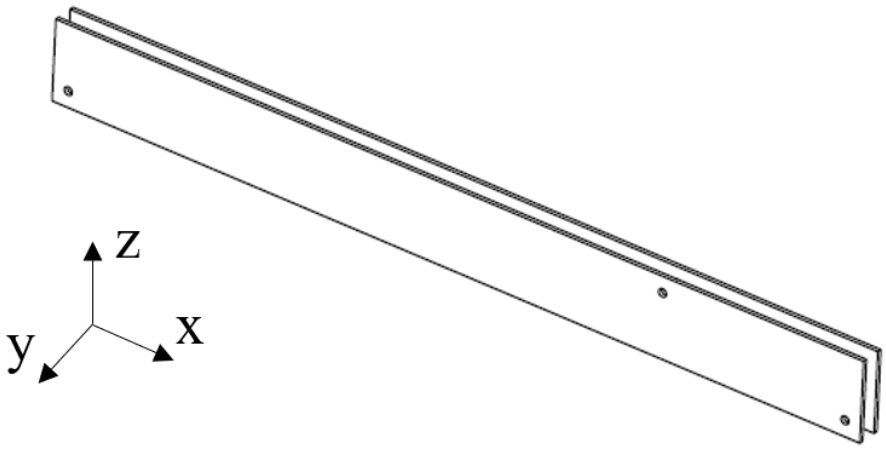

Figure 3.5 Chordwise and Spanwise Spreader Beam Design [27].

The chosen thickness and height of the beam was determined based on the availability and cost of the material supplier. To mitigate shear tear-out failure, all holes were drilled 2 diameters from the edge. As all drilled holes were 0.25 inches, each hole center was drilled 0.5 inches from the nearest edge. Considering the length of the beams, additional material was added to ensure 0.5 inches of material was present on each side. Regarding the initial beam dimensions, a stock material with a thickness of 0.25 inches and height of 5 inches was chosen for the most critical beam, SWB1. For all other spreader beams a thickness of 0.125 inches and height of 2 inches was chosen. Such whiffletree configuration is presented in Figure 3.6 and Figure 3.7.

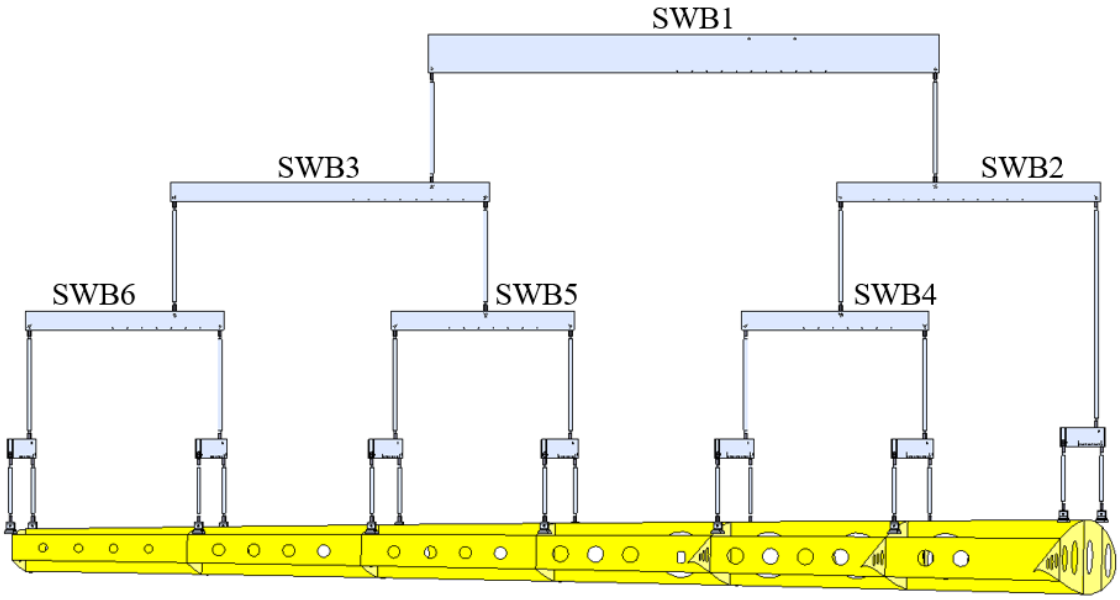

Figure 3.6 Whiffletree Spanwise Spreader Beams.

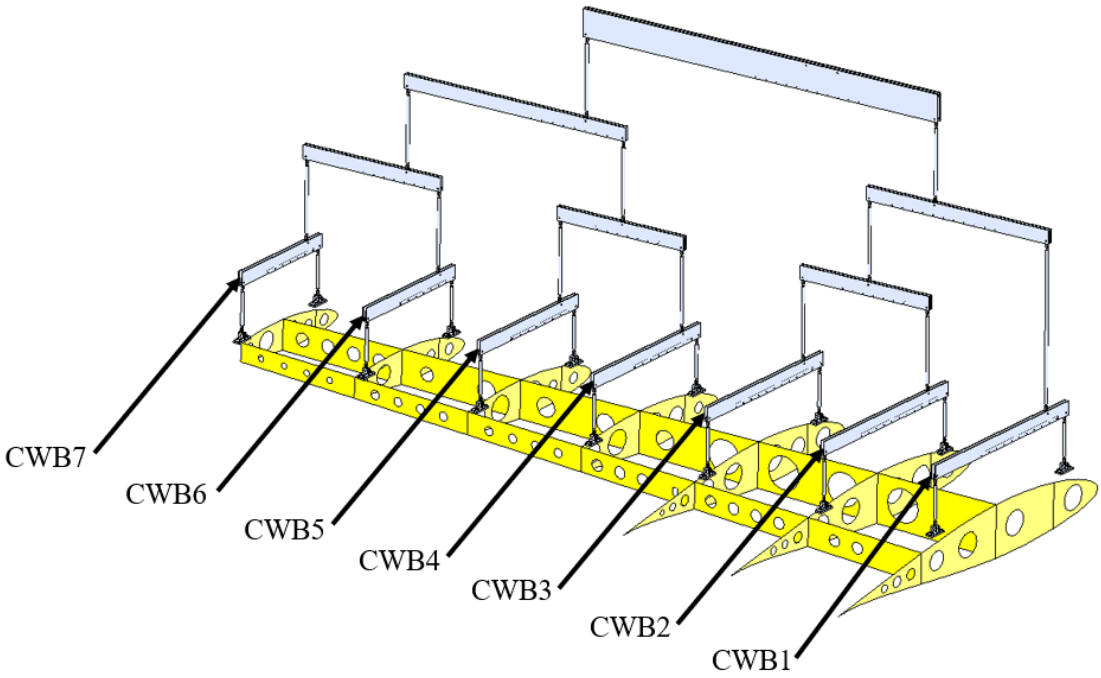

Figure 3.7 Whiffletree Chordwise Spreader Beams.

Utilizing the described beam dimensions, the section properties were calculated to determine the margin of safety for each spanwise and chordwise beam. Moreover, the section properties were calculated using the cross section at the location of the highest bending moment determined previously using Figure 3.4 and Equation 3.3. As such, the location of the neutral axis and the moment of inertia about the neutral axis was calculated using the following equations:

$$Y = \frac{\sum(A\bar{y})}{A_{Total}} \tag{3.4}$$

$$I_{x,ref} = \sum I_{NA} + \sum A\bar{y}^2 \tag{3.5}$$

$$I_{x,NA} = I_{x,ref} - (A_{Total} \times Y^2) \tag{3.6}$$

Additionally, to calculate the theoretical bending stress experienced by the beam, the distance between the top and bottom of the beam and the neutral axis was utilized. The cross section of the most critical beam of the whiffletree, CWB1, is presented in Figure 3.8.

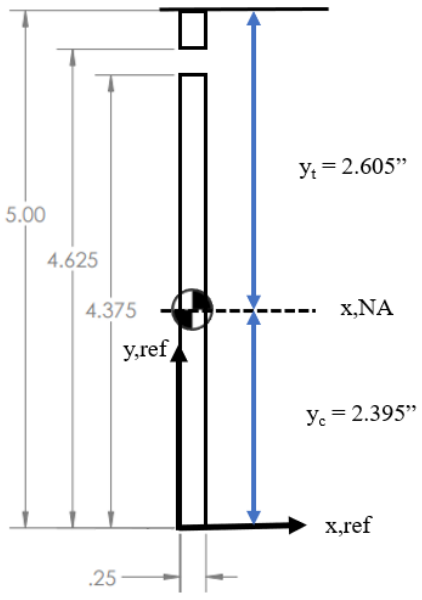

Figure 3.8 The Cross Section of One Beam of SWB1.

To calculate the margin of safety for each beam, the theoretical bending stress was calculated for both tension, using Equations 3.7 and 3.8, and compression, using equations 3.9 and 3.10.

$$f_{b,t} = \frac{M_x y_t}{I_x} \tag{3.7}$$

$$M.S. = \frac{F_{tu}}{(1.5) \times f_{b,t}} - 1 \tag{3.8}$$

$$f_{b,c} = \frac{M_x y_c}{I_x} \tag{3.9}$$

$$M.S. = \frac{F_{cy}}{f_{b,c}} - 1 \tag{3.10}$$

Following the same procedures for each spanwise and chordwise beam, the resulting margin of safeties for bending in compression and tension are presented in Table 3.5 and Table 3.6.

Table 3.5 Margin of safety for whiffletree spanwise beams in bending.

Beam	**M_x (in-lb)**	**$f_{b,t}$ (psi)**	**$f_{b,c}$ (psi)**	**Tensile Bending M.S.**	**Compressive Bending M.S.**
SWB1	5080	5654	5197	5.2	5.5
SWB2	1626	15153	13259	1.3	1.6
SWB3	709	6608	5782	4.3	4.9
SWB4	767	7146	6253	3.9	4.4
SWB5	580	5408	4732	5.5	6.2
SWB6	95	887	776	38.4	42.8

Table 3.6 Margin of safety for whiffletree chordwise beams in bending.

Beam	**M_x (in-lb)**	**$f_{b,t}$ (psi)**	**$f_{b,c}$ (psi)**	**Tensile Bending M.S.**	**Compressive Bending M.S.**
CWB1	636	5930	5189	4.9	5.6
CWB2	540	5030	4401	6.0	6.7
CWB3	446	4156	3636	7.4	8.4
CWB4	351	3272	2863	9.7	10.9
CWB5	306	2854	2497	11.3	12.6
CWB6	92	860	753	39.7	44.2
CWB7	26	239	209	145.6	161.8

Considering such margin of safeties, is evident that each spreader beam in the whiffletree structure will be sufficient for resisting failure due to the bending stress concentrations during testing. In addition to bending stress, it is also important to consider the bearing stress and stress concentration acting on the holes of the beams during testing. To determine the stress concentration acting at the spanwise and chordwise spreader beams, Peterson's method was implemented which incorporates a stress concentration factor from previously tested specimen to produce a theoretical maximum stress. The equation used to determine the stress concentration for holes in thin beams in presented in equation 3.11.

$$\sigma_{max,B} = K_{tgB}(6\,M_{max}/(H^2 t)) \tag{3.11}$$

The resulting hole stress concentrations along with their margin of safeties for the spanwise and chordwise beams are presented in Table 3.7 and Table 3.8 respectively.

Table 3.7 Margin of safety for whiffletree spanwise beams hole stress concentrations.

Beam	**$\sigma_{max,B}$ (psi)**	**Hole Stress Concentration M.S.**
SWB1	23910	0.46
SWB2	27344	0.28
SWB3	11924	1.94
SWB4	12895	1.71
SWB5	9758	2.59
SWB6	1601	20.86

Table 3.8 Margin of Safety for whiffletree chordwise beams hole stress concentrations.

Beam	**$\sigma_{max,B}$ (psi)**	**Hole Stress Concentration M.S.**
CWB1	10701	2.27
CWB2	9077	2.86
CWB3	7499	3.67
CWB4	5905	4.93
CWB5	5149	5.80
CWB6	1552	21.54
CWB7	431	80.25

Considering the results for the hole stress concentration analysis, it is evident that each beam will be sufficient to maintain structural integrity during testing as each calculated margin of safety is greater than zero. In addition to bending stress and hole stress concentration analysis, tear out and bearing stress on the beams must also be considered, including the shear present on the fastening bolts. To determine the tear out stress, a conservative approach was taken by using a

smaller area along the direction of loading rather than the area at a 40-degree angle. The theoretical calculation utilized for determining tear out stress is presented in equation 3.12.

$$f_s = \frac{P}{2tx'} \tag{3.12}$$

Thus, the maximum theoretical tear out stress and margin of safety was calculated for each spanwise and chordwise beam, the results are presented in Table 3.9 and Table 3.10 respectively.

Table 3.9 Margin of safety for whiffletree spanwise beams tear out stress.

Beam	**f_s (psi)**	**Tear Out Stress M.S.**
SWB1	1980	12.6
SWB2	2496	9.8
SWB3	1464	17.4
SWB4	1572	16.2
SWB5	1212	21.3
SWB6	252	106

Table 3.10 Margin of safety for whiffletree chordwise beams tear out stress.

Beam	**f_s (psi)**	**Tear Out Stress M.S.**
CWB1	1848	13.6
CWB2	1668	15.2
CWB3	1476	17.3
CWB4	1248	20.6
CWB5	1176	22.0
CWB6	384	69.3
CWB7	120	224

Thus, even with a conservative approach, the tear out stress experienced by each beam will be sufficient. Considering the bearing stress acting on each beam, the force acting on the largest cross-sectional area of the hole, at the center, was utilized. The calculation for determining the bearing stress at the most critical hole on each spreader beam on the whiffletree is presented in equation 3.13.

$$f_{br} = \frac{P}{td} \tag{3.13}$$

There results for the bearing stress acting on each beam is shown in Table 3.11 and Table 3.12 along with their accompanying margin of safeties.

Table 3.11 Margin of safety for whiffletree spanwise beams bearing stress.

Beam	**f_{br} (psi)**	**Bearing Stress M.S.**
SWB1	15840	2.8
SWB2	9984	5.0
SWB3	5856	9.2
SWB4	6288	8.5
SWB5	4848	11.4
SWB6	1008	58.5

Table 3.12 Margin of safety for whiffletree chordwise beams bearing stress.

Beam	**f_{br} (psi)**	**Bearing Stress M.S.**
CWB1	1848	13.6
CWB2	1668	15.2
CWB3	1476	17.3
CWB4	1248	20.6
CWB5	1176	22.0
CWB6	384	69.3
CWB7	120	224

Considering the margin of safety for each beam regarding bearing stress, it is evident that each beam was sufficient for the designed distributed whiffletree load. Alas, it is determined that the spreader beams will not encounter material failure due to the stress experienced during loading.

In additional to failure due to stress concentrations, buckling must also be considered. In previous analysis completed during the early development of this project, buckling analysis for SWB1 was preformed using Femap NX NASTRAN. The result of such analysis is presented in Figure 3.9.

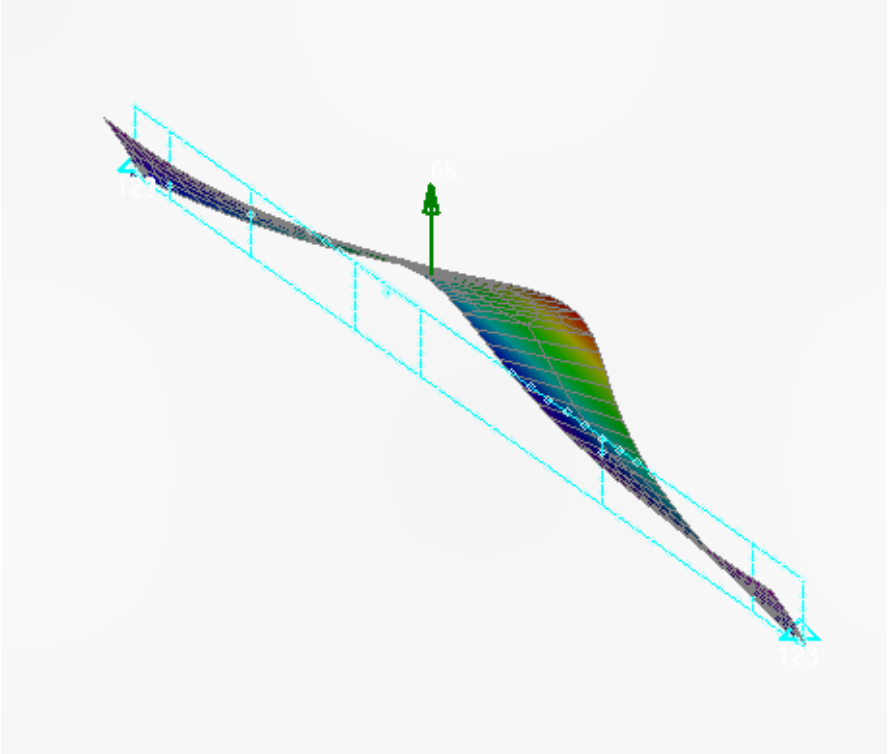

Figure 3.9 Femap NX NASTRAN Out of Plane Buckling of SWB1 [27].

As such, it is evident that out of plane buckling is experienced by SWB1 and likely experienced by the other spreader beams. To mitigate this problem, a rectangular rod was used to attach the two thin beams together using multiple rivets to create a cross section like that of a C-channel. Such implementation also changed location of the neutral axis and thus, bending stress analysis was repeated using equations 3.4-3.10 and the new cross section shown in Figure 3.10.

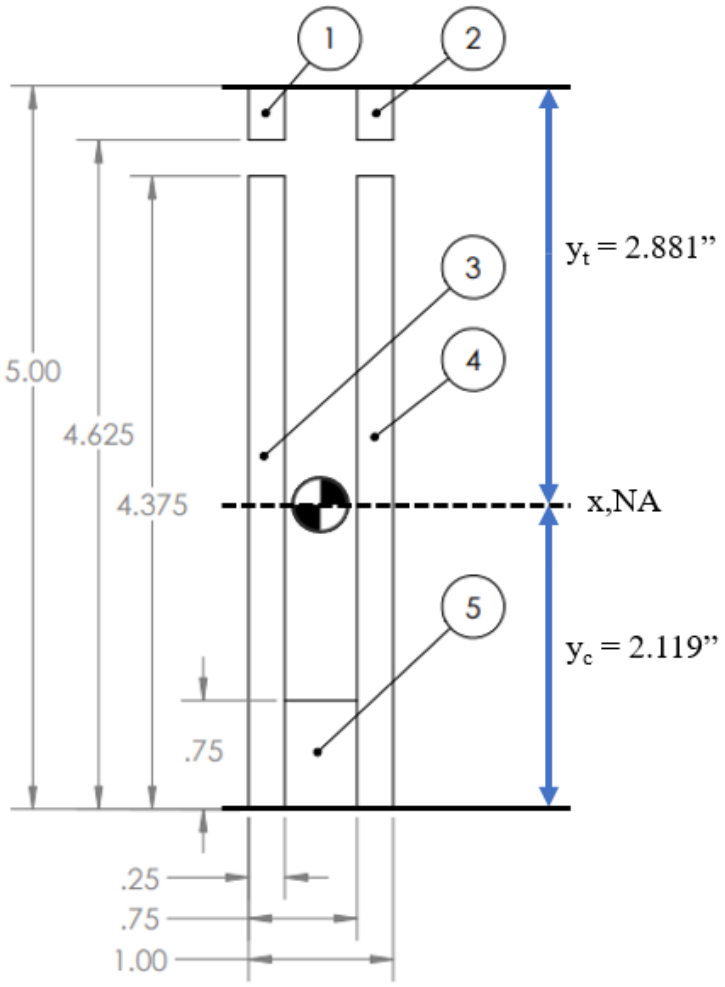

Figure 3.10 Cross Section of SWB1 Including Rectangular Bar.

Using the described parameters, the maximum bending stress and margin of safety was calculated for each spanwise and chordwise beam to ensure the modified cross section will be sufficient in handling the compressive and tensile bending stress experienced during testing. The results for these calculations are shown for each spanwise and chordwise spreader beam in Table 3.13 and Table 3.14 respectively.

Table 3.13 Margin of safety for modified whiffletree spanwise beams in bending.

Beam	**M_x (in-lb)**	**$f_{b,t}$ (psi)**	**$f_{b,c}$ (psi)**	**Tensile Bending M.S.**	**Compressive Bending M.S.**
SWB1	10159	12503	9198	1.8	2.7
SWB2	3252	32247	24576	0.1	0.4
SWB3	1418	14063	10717	1.5	2.2
SWB4	1533	15207	11589	1.3	1.9
SWB5	1160	11508	8771	2.0	2.9
SWB6	190	1888	1439	17.5	22.6

Table 3.14 Margin of safety for modified whiffletree chordwise beams in bending.

Beam	**M_x (in-lb)**	**$f_{b,t}$ (psi)**	**$f_{b,c}$ (psi)**	**Tensile Bending M.S.**	**Compressive Bending M.S.**
CWB1	1273	12620	9618	1.8	2.5
CWB2	1079	10705	8158	2.3	3.2
CWB3	892	8844	6740	3.0	4.0
CWB4	702	6964	5308	4.0	5.4
CWB5	612	6073	4628	4.8	6.3
CWB6	185	1831	1395	18.1	23.4
CWB7	51	508	387	67.9	86.8

Regarding the margin of safety for the whiffletree beams under tensile and compressible bending, the component will not fail due to bending. While the margin of safety for SWB2 is close to 0, the part should remain operable if the designed load is not substantially surpassed.

3.1.3 Analysis of the Connecting Rods

When considering the overall construction of the whiffletree, the development and analysis of the connecting rods is of upmost importance as failure in the rods would result in catastrophic failure of the overall system. As such, the rods were designed to utilize high strength spherical bearing heads attached to threaded rod ends and riveted to hollow aluminum rods. An assembled drawing of the connecting rods is presented in Figure 3.11.

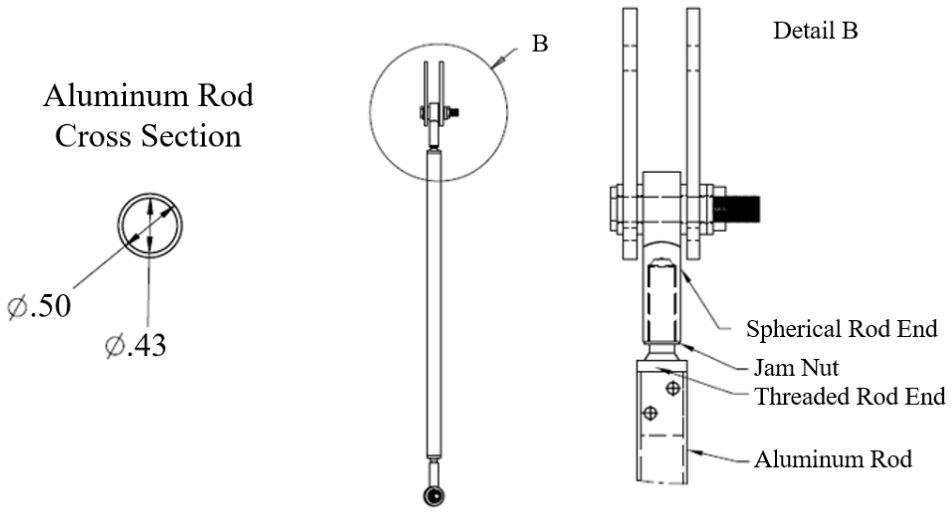

Figure 3.11 Whiffletree Connecting Rods [27].

To verify the structural integrity of the rod structure, the rods tensile strength and margin of safety are defined. As the rod will only be in uniaxial tension, the compressive strength of the rod is not required to verify the integrity of the rod structure. To calculate the theoretical tensile stress experienced by the rod equation 3.14 is utilized.

$$\sigma_t = \frac{P}{A} = \frac{P}{\pi\left(\frac{d}{2}\right)^2} \tag{3.14}$$

As the SWB1 will not utilize the described rod on the critical center hole, the highest tensile load experienced by the connection rod will be in SWB2. As such the highest load experienced by the connection rod previously calculated when developing the whiffletree structure is 416 lbs. As such, the results for the tensile analysis of the connecting rod are shown in Table 3.15.

Table 3.15 Margin of safety for the developed connection rods in tension.

Component	**P (lb)**	**σ_t (psi)**	**Tensile M.S.**
Connection Rod	416	8136	3.3

Considering these results, the connecting rods will not fail due to tensile stress. In addition to tensile stress, the shear stress and bearing stress experienced by the two rivets holding the rods to the spherical bearing heads at each end must be analyzed. The load acting on each of the four rivets used to adhere each rod is present below. To simplify calculations, the rod end is considered solid. The cross section and loads acting in shear on the component is presented in Figure 3.12.

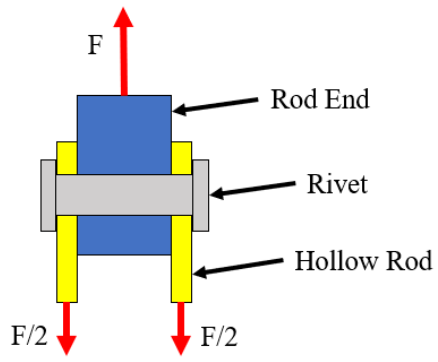

Figure 3.12 Shear Forces in Connecting Rods.

As multiple rivets are in shear, it is assumed that the applied theoretical max load is split among each rivet. As such, each rivet experiences a designed load of 330 lbs. in double shear. To determine the margin of safety for the rivets, the shear strength, bearing strength, and strength factor was interpolated from MIL-HDBK5 [28]. These values are shown in Table 3.16. To determine the margin of safety for the rivets in bearing, equations 3.15 and 3.16 are implemented, where the maximum load experienced by a single rivet is 104 lbs.

$$P_{bry} = \frac{Bearing\ Strength \times F_{bry}}{100000} \tag{3.15}$$

$$Bearing\ Stress\ M.S. = \frac{P_{bry}}{Max\ Load\ on\ Single\ Rivet} - 1 \tag{3.16}$$

The margin of safety due to the shear acting on the rivets was calculated using equation 3.17 where the maximum load experienced is 330lbs.

$$Shear\ Stress\ M.S. = \frac{4 \times Shear\ Strength \times\ Strength\ Factor}{Maximum\ Load} - 1 \tag{3.17}$$

The resultant bearing stress and shear stress margin of safeties for the rivets used in the connecting rods are presented in Table 3.16.

Table 3.16 Margin of safety for modified whiffletree rod rivets in shear and bearing

Component	**Bearing Strength (lb)**	**Shear Strength (lb)**	**Strength Factor (lb)**	F_{bry} **(psi)**[28]	**Shear Stress M.S.**	**Bearing Stress M.S.**
Rod Rivets	336	217	0.846	56000	1.23	0.14

Considering such analysis, it is evident that the average shear stress and bearing stress acting on the connecting rod rivets is sufficient to withstand the designed loads. Regarding the development and assembly of the whiffletree structure, the whiffletree beams and internal bar structures were developed using the KOMO CNC Mill shown in Figure 3.13. To ensure all of the components were produced with high accuracy, each product was modeled using SolidWorks and

a G-Code was written to automate milling process. After milling the holes for each beam and internal bar, a rivet gun was used to rivet the components together.

Figure 3.13 KOMO CNC Milling Machine.

The connecting rods were developed similarly using the Track CNC Mill. Such equipment allowed for the holes in the rods that were riveted to the threaded rod ends to be replicated exactly for each rod and reduced overall manufacturing error. After riveting the threaded rod ends to the hollow rods, the spherical bearing heads were screwed onto the threaded rods and held in place using a jam nut.

3.1.4 Wing Pad Connectors and Wing Bonding

Ensuring a secure connection to the wing surface is crucial for ensuring the designed load is transferred to the wing rib effectively. When developing the connection point from the whiffletree structure to the wing surface, two alternative methods were discussed. Namely, a wooden brace encasing the rib structure and a connection pad adhered directly to the wings surface atop the rib section.

Considering the brace structure, it is evident that the accuracy of the machined brace will significantly affect the load distribution applied to the wing surface. As such, any deformities between the connection brace and the wing structure could result in significant stress concentration on the wing skin. Aside from such difficulty, a properly machined brace structure would be ideal as the load would be distributed along the entire rib structure and not directly on any rivets.

Alternatively, a connection pad adhered directly to the wings surface was another potential candidate for connecting the whiffletree to the rib structures. Such method would allow for a significant reduction in production time as no intricate brace structures would need to be machined. Although simple, it is evident that a large point load adhered to the wing surface poses the risk of applying unintended load to the skin of the wing that could result in a variation in the strain along the wings surface between point loads. Another crucial factor to consider is the adhesion to the surface of the wing. As the load is concentrated, it is crucial to ensure that the rivets in tension will support the applied load.

While both methods were deemed reliable methods of applying the designed quasi-static load, the latter method of a connection pad was ultimately chosen due to its straightforward design and method of manufacturing. As such, a connection pad was designed to attach to the whiffletree connecting rod using a spherical bearing head. A computer-generated model of the whiffletree connecting pad without any bolts, nuts, or machine screws is shown in Figure 3.14. Considering

such, the connecting pads were developed in three parts, two L-shaped angle beams, and a singular aluminum plate. The aluminum plate is adhered to the angle beams using countersunk machine screws such that the bottom surface lies flush with the wing surface. A high strength bolt is used to connect the two angled beams to the spherical bearing head and thus, the rest of the whiffletree assembly.

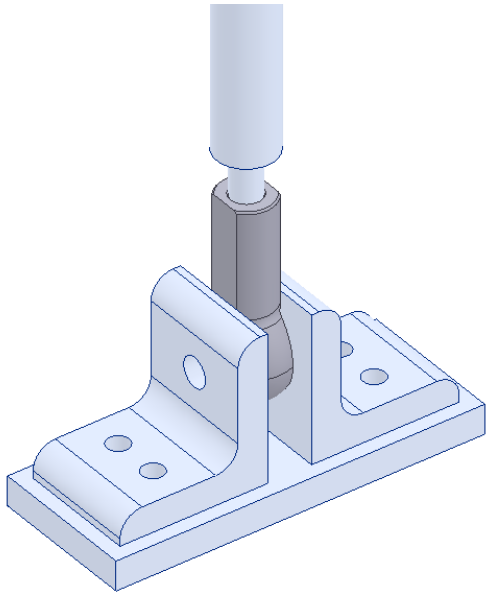

Figure 3.14 Whiffletree to Wing Connecting Pad

Considering this conceptual design, analysis was performed to ensure that the part did not fail during loading. As the highest load this part will experience is a tensile load acting about the connection point along the front stringer at rib 1, such loading was used to verify the structural integrity of the component. Particularly, the tensile load present in the machine screws connecting the aluminum plate to the angled beam is to be considered. As there exists a prying load acting on the machine screws, this load must also be considered when performing a tensile stress analysis.

Performing initial tensile analysis of each machine screw, the load applied from the connecting rod is assumed to be spread evenly among each screw. As there is 132 lbs acting upon the front stringer, each machine screw will realize 33 lbs in tension. Utilizing equation 3.8 and equation 3.14 the tensile load and margin of safety for each bolt is shown in Table 3.17.

Table 3.17 Machine screw tensile stress analysis.

Component	T_p **(lb)**	σ_t **(psi)**	**Tensile M.S.**
Machine Screw	33	1195.13	28.3

As the mechanical strength of each screw is sufficient for resisting the tensile load, the required thickness of the angle beam in calculated to ensure the part will not yield due to the prying force. To complete this analysis, equation 3.18 is implemented [29].

$$t_{req} = \sqrt{\frac{8T_p x'}{KF_{ty}}} \tag{3.18}$$

The resultant thickness required to prevent yield due to the prying force is presented in Table 3.18.

Table 3.18 Connecting pad prying stress analysis.

Component	T_p **(lb)**	F_{ty} **(psi)** [28]	t_{req} **(in)**	t_{actual} **(in)**
Connecting Pad	33	35000	0.068	0.25

Comparing the required bracket thickness to the actual thickness of the designed bracket, it is evident that the designed component will not fail due to prying. Considering such, the method of adhesion to the surface of the light sport aircraft wing must be discussed. Due to budget and time constraints, methods of adhesion were restricted to adhesive tape and epoxies that were available during project development. Namely, acrylic adhesive 3M VHB Tape 4905 and an Aeropoxy two-

part PR2032 and PH3665 epoxy resin and hardener. As both adhesion methods were not specially designed for bonding metal, experimental analysis was performed to evaluate the adhesives' ability to bond the connecting pad to a flat aluminum surface. During preliminary experimentation, a 24-hour static tensile load was applied to the test article as shown in Figure 3.15.

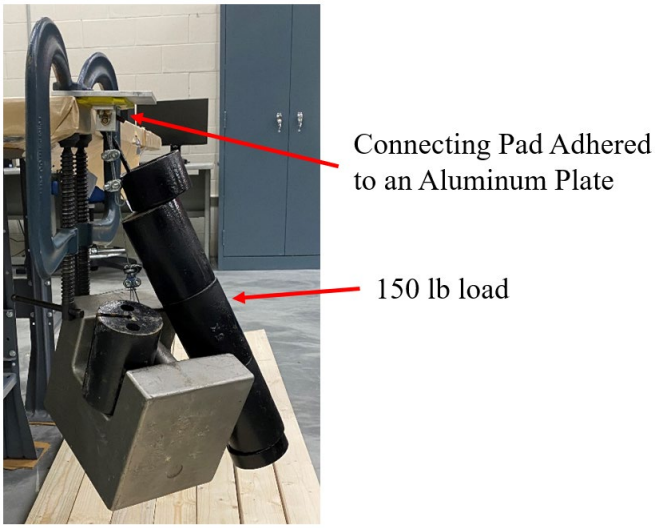

Figure 3.15 Connecting Pad 24-Hour Static Tensile Test.

Following preliminary experimentation, the 3M VHB Tape 4905 failed in tension after approximately 15 minutes of loading. Comparatively, the Aeropoxy two-part PR2032 and PH3665 epoxy resin and hardener did not fail after 24 hours. Inspecting the latter after experimentation revealed no noticeable changes to the test article due to the applied load. Thus, the Aeropoxy two-part PR2032 and PH3665 epoxy resin and hardener was utilized for experimentation as the primary method of bonding the connecting pads to the wing surface.

While bonding the connecting pads to the wing surface, it was evident that the two-part epoxy paint previously applied to the surface of the wing would significantly affect the bond strength as

such paint is not designed to resist tensile loads. To avoid this problem, Jasco paint and epoxy remover was utilized to remove the paint from the surface of the wing. After such, the wing was prepped for bonding using 150-grit and 400-grit sandpaper and cleaned for adhesion using acetone and water.

As there was a significant thickness required for the bonding of the connecting pad to the surface due to the rivets on the surface of the wing. A dam was created around each connection point using yellow sealant tape and carbon fiber particles were added to the epoxy solution during bonding to increase the viscosity. Such method was an effective way to bond and mitigate the effect of the rivets as well as the uneven surface bonding connections due to the curvature of the wing. A completely bonded connection pad and assembly including the spherical bearing head and connecting rod is shown in Figure 3.16.

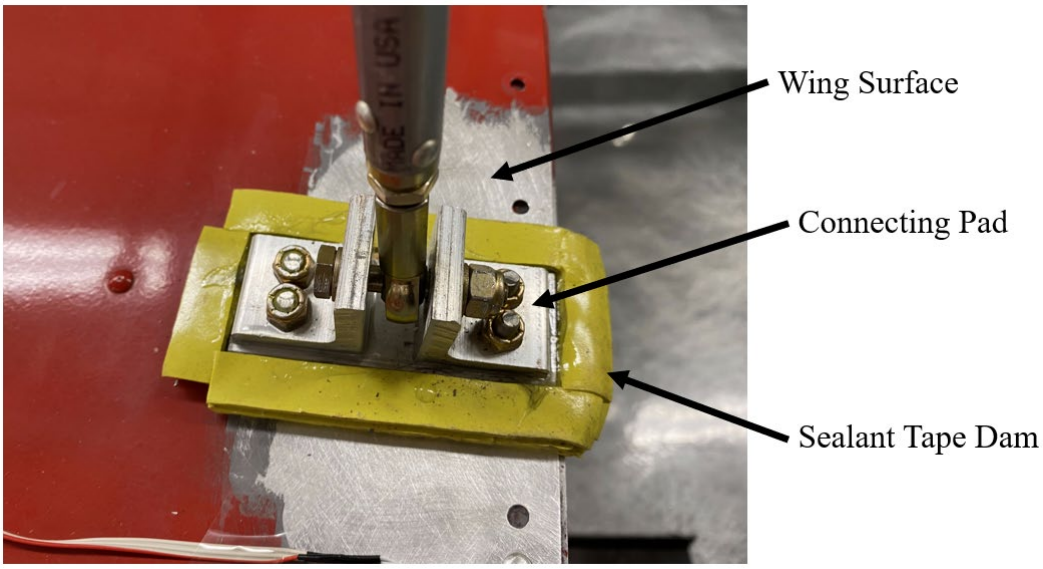

Figure 3.16 Connecting Pad Adhered to the Wing Surface.

During the development of the connection pad, it was evident that the connection rod bolt was required to be removed while curing to reduce the load on the epoxy and allow sufficient epoxy above the rivets. As the machine screw threads were too long to allow for the bolt to be removed, a band saw was used to remove the excess screw threads and allow for the machine screws to fit. All other components were milled and drilled to the designed dimensions using a Trak K3 Milling Machine, shown in Figure 3.17.

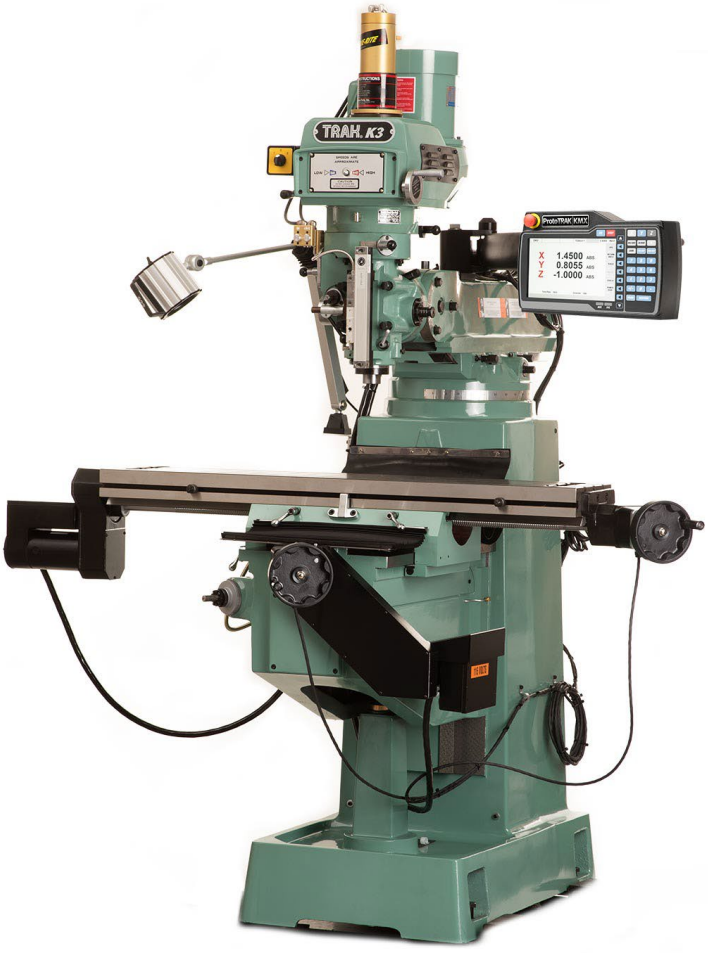

Figure 3.17 Trak K3 Milling Machine [30].

3.1.5 Pulley System and Tangs

As the load will be applied to the whiffletree using a hydraulic ram that is located next to the whiffletree, it was evident that a pulley cable and tang system must be designed to redirect the load atop the whiffletree. The anatomy of this system is presented in Figure 3.18. To design such system, the first thing that must be realized is the load of the cable and phenolic pulleys. Considering the 660-pound load that will be applied, a MS20220-4 Phenolic pulley was chosen, with a load limit of 2500 lbs in addition to a 1/8" cable with a designed tensile strength of 1760 lbs. The first phenolic pulley was adhered to the gusset using the designed tang to direct the load without interfering with the whiffletree structure. To position the load at the top of the whiffletree a beam clamp with an operational load of 1000 lbs in tension was utilized to secure the second phenolic pulley.

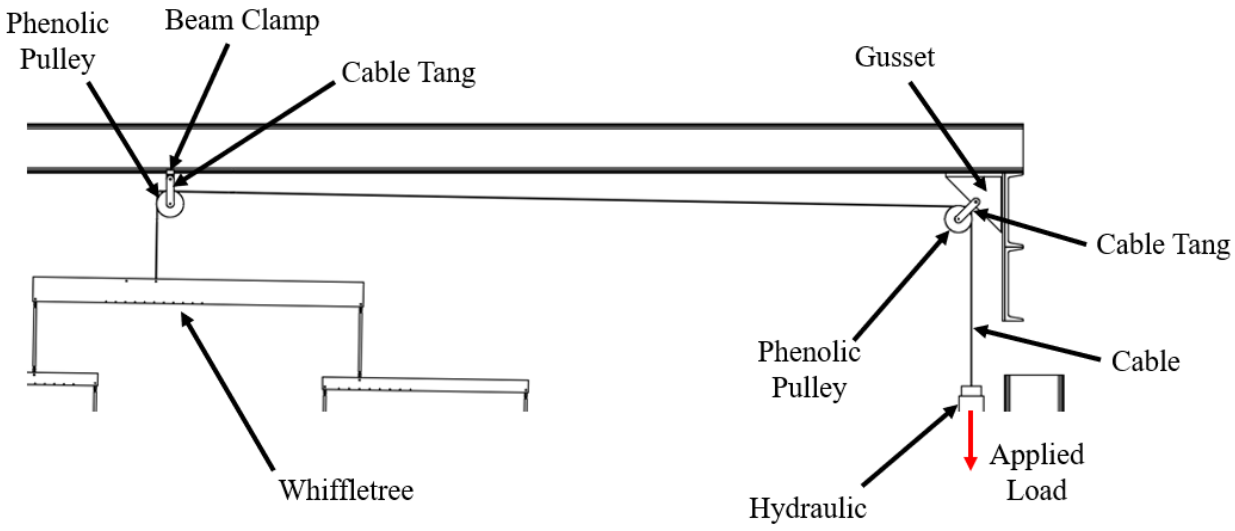

Figure 3.18 Hydraulic Pulley Cable System.

As the pulley system was designed specifically for this system, analysis was completed on the aluminum pulley tangs to ensure they will not fail during operation. Namely, tensile failure and shear bearing failure of the tangs was completed. Shear-tear-out failure occurs along a 40-degree

angle on each side of the pin. Such modes of failure are shown graphically using the normal view of the tang article in Figure 3.19.

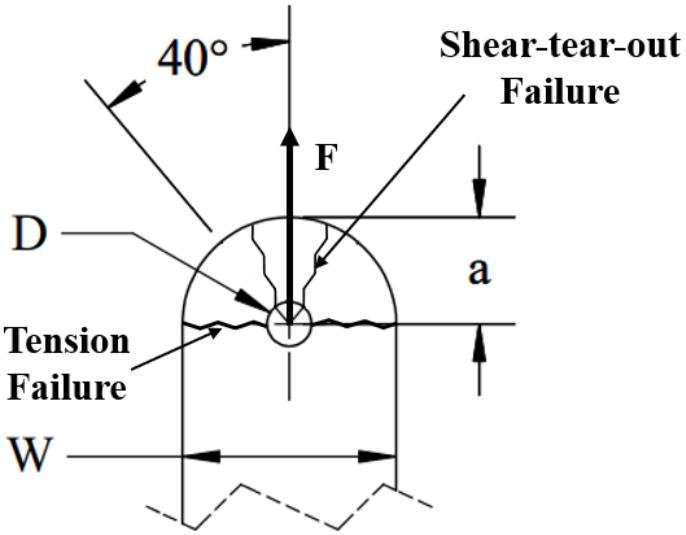

Figure 3.19 Lug Shear-tear-out and Tension Failures in Tang.

To evaluate the tensile failure of the tang, the tensile stress in the direction of the applied load, F_t is determined using equations 3.19 and 3.20. Additionally, equation 3.21 was utilized to determine the margin of safety for tensile failure. To determine the shear-bearing efficiency factor, the mechanical and geometrical properties of the tang are utilized with NASA-TM-X-73305 Astronautics Structures Manual charts relating such properties to an efficiency factor [31].

$$F_t = \frac{P_t}{k_t \times A_t} \tag{3.19}$$

$$A_t = (W - D) \times t \tag{3.20}$$

$$M.S. = \frac{F_{tu}}{(1.5) \times F_t} - 1 \tag{3.21}$$

Furthermore, to calculate the shear bearing failure for the tang, equations 3.22 and 3.23 are introduced. The margin of safety for the shear bearing failure of the tang is evaluated using equation 3.24. To determine the shear-bearing efficiency factor, NASA-TM-X-73305 Astronautics Structures Manual charts were implemented [31].

$$f_{br} = \frac{P_{br}}{k_{br} \times A_{br}} \tag{3.22}$$

$$A_{br} = D \times t \tag{3.23}$$

$$M.S. \ = \frac{F_{bru}}{(1.5) \times f_{br}} - 1 \tag{3.24}$$

Using the aforementioned equations, the tensile and shear-tear-out modes are calculated and their results, along with their respective margin of safeties, are presented in Table 3.19. Analyzing these results, it is evident that the tang will be sufficient for the designed load of the whiffletree.

Table 3.19 Tensile and shear-tear-out tang stress analysis.

Component	σ_t **(psi)**	f_{br} **(psi)**	k_t	k_{br}	F_{bru} **(psi)**[28]	P_{bru} **(psi)**[28]	**Tensile M.S.**	**Shear-Tear-Out M.S.**
Pulley Tang	17101	7680	0.13	1.1	42000	67000	0.64	4.8

To complete the development and analysis of the pulley system, the angle between the phenolic pulley positioned on the gusset and the phenolic pulley secured to the beam clamp must be discussed to ensure that proper tang clearance exists. As such, the offset angle present between the gusset pulley and beam clamp pulley was evaluated, as shown in Figure 3.20. The purpose of analyzing the offset angle is to determine the equilibrium location of the gusset pulley during operation.

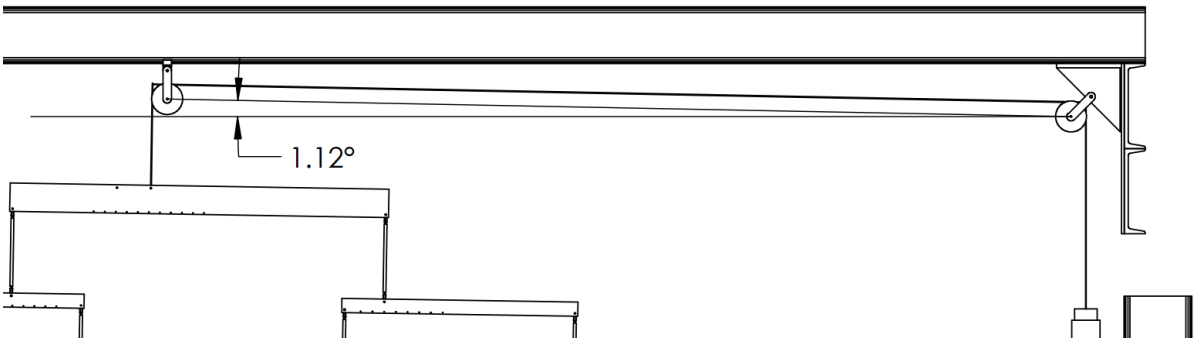

Figure 3.20 Tang Horizontal Cable Misalignment.

To evaluate the equilibrium angle, a static analysis was performed to establish the offset angle in which the moments due to the tensile loads acting on the pulley will be zero. As such, a relationship between the pulley tang and cable geometry must be determined. To further break down the loads acting on the gusset pulley, a free body diagram was established and is presented in Figure 3.21.

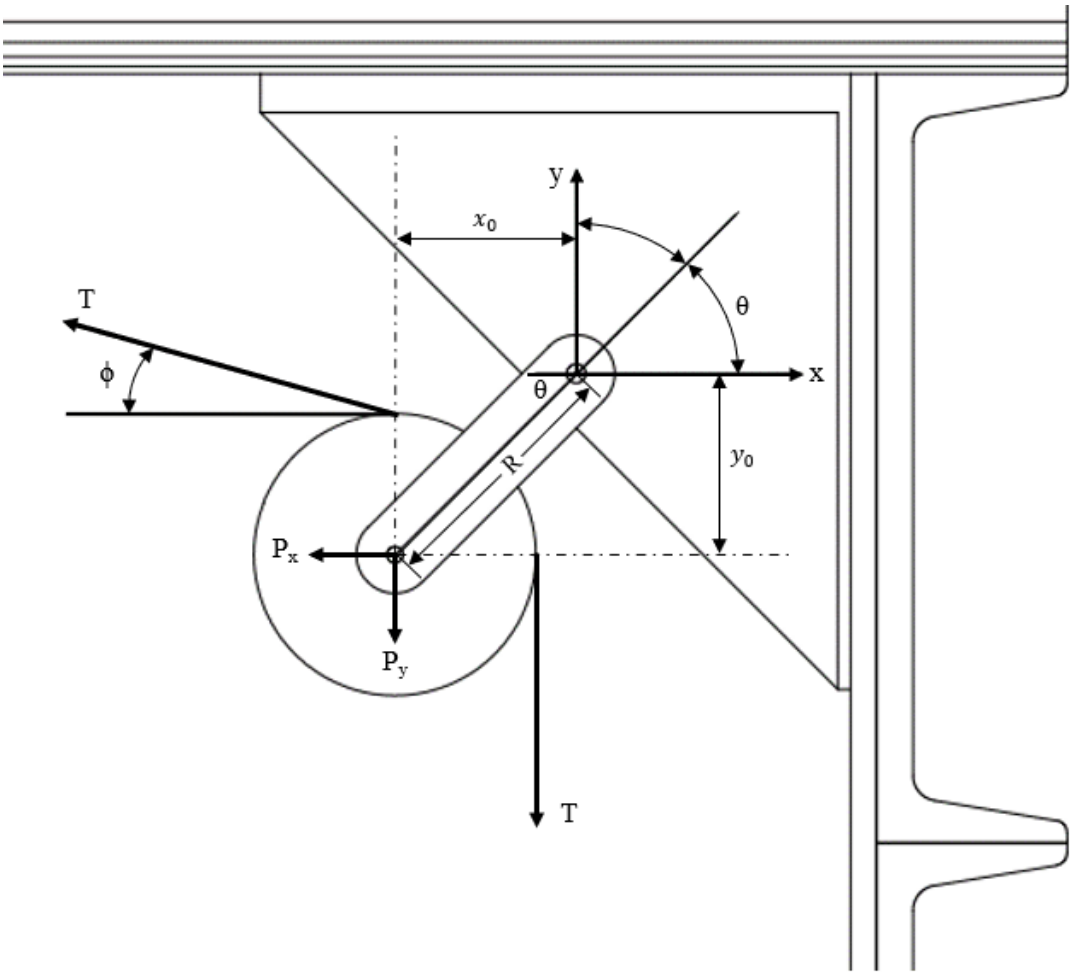

Figure 3.21 Free Body Diagram of Gusset Pulley.

From such diagram, a relationship between the tensile cable loads and the center of the phenolic pulley was established. Additionally, a relationship between the moment arm acting about the gusset and the loads acting at the center of the phenolic pulley was determined. These relationships are presented in equations 3.25, 3.26, 3.27, and 3.28.

$$x_0 = R\,cos(\theta) \tag{3.25}$$

$$y_0 = R\,sin(\theta) \tag{3.26}$$

$$P_x = T\,cos(\phi) \tag{3.27}$$

$$P_y = T - T\sin(\phi) \tag{3.28}$$

Using the static assumption that the moment taken about the gusset hole is zero, a relationship can further be established between the cable angle, ϕ, and equilibrium offset angle. This relationship is demonstrated in equation 3.29.

$$tan^{-1}(\theta) = \frac{cos(\phi)}{1 - sin(\phi)} \tag{3.29}$$

Adapting such relationship to the theoretically offset angle determined from the computer-generated model, the equilibrium angle can be realized. These results are shown in Table 3.20.

Table 3.20 Gusset tang equilibrium alignment.

$\boldsymbol{\phi}$, **Horizontal Cable Mis-Alignment (Degrees)**	$\boldsymbol{cos(\phi)}$	$\boldsymbol{sin(\phi)}$	$\boldsymbol{tan^{-1}(\theta)}$	$\boldsymbol{\theta}$, **Equilibrium Angle (Degrees)**
1.12	0.9998	0.0196	1.0197	45.56

Considering the determined equilibrium angle, it is evident that there exists an acceptable clearance between the pulley tang and the gusset above the hydraulic ram. During experimentation, the equilibrium angle was remarkably close to the theoretical result, shown in Figure 3.22.

Figure 3.22 Equilibrium Position of Pulley System at Gusset.

3.2 Finite Element Analysis Model

To develop the described finite element model, the surface geometry of the aircraft wing structure was designed using CATIA V5 following the geometric properties established using drawings of the experimental light sport aircraft. After such, the modeled surfaces were transferred to Femap NX NASTRAN where material properties for each surface were established using the geometry described in Table 3.21.

Table 3.21 Femap NX NASTRAN plate properties.

Component	**Material**	**Thickness (in)**	**Idealized Area (in^2)**
Forward Spar Web	Al 6061-T6	0.040	N/A
Aft Spar Web	Al 6061-T6	0.032	N/A
Rib Web	Al 6061-T6	0.032	N/A
Forward Spar Fitting	Al 6061-T6	0.375	N/A
Aft Spar Fitting	Al 6061-T6	0.125	N/A
Skin	Al 6061-T6	0.032	N/A
Stringers	Al 6061-T6	0.032	0.072

Utilizing these properties, the modeled surfaces were meshed in Femap NX NASTRAN. The resultant model is shown in Figure 3.23. After establishing the model, the theoretical loads acting on the front stringer and aft spar were applied along each rib. Additionally, the pinned lug constraints were applied to the forward and aft spar fittings.

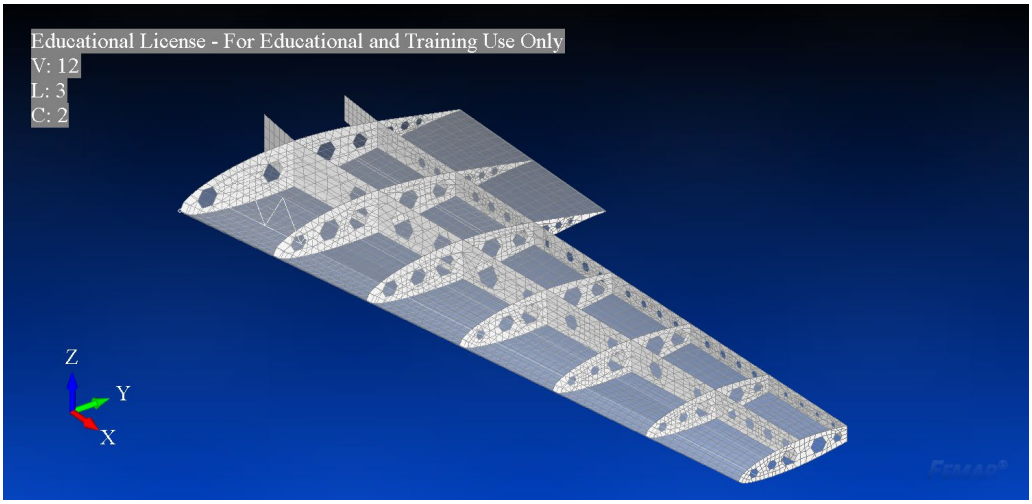

Figure 3.23 Femap NX NASTRAN Aircraft Wing Model.

3.3 Collected Data Sources and Devices

The described section will establish a basis for the data types that will be collected during the experimental process of this report and describe the theoretical understanding of the implemented sensors. As such, this section will describe the implementation of strain gauges, force cells, and finite element modeling used to generate data that will be described in the analysis of this report.

3.3.1 Strain Gauges

Strain gauges are a staple for accurately measuring strain on an object in the aerospace industry. Strain gauges operate by evaluating the elongation of a material by measuring the change in resistance of a foil pattern printed on the strain gauge. Operation of a typical uniaxial foil strain gauge is presented in Figure 3.24. While there exist many different types of strain gauges, this report will only focus on utilizing uniaxial strain gauges as the strain that will be measured is assumed due primarily to uniaxial bending.

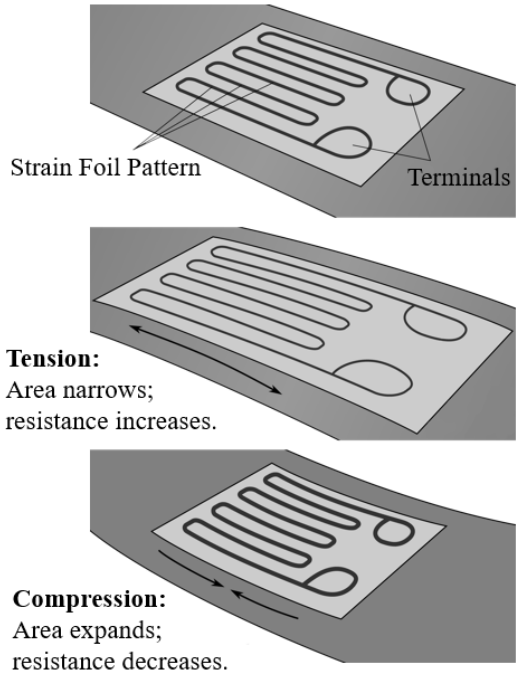

Figure 3.24 Uniaxial Strain Gauge Operation.

As stress is the primary value that will be obtained from experimentation, Hooke's law will be implemented. Hooke's law utilizes the young's modulus of a material to convert the measured microstrain to the stress experienced by the structure. The locations in which the strain gauges are adhered to the experimental aircraft wing's surface is presented in Figure 3.25. These locations were chosen based off of preliminary finite element analysis which indicated the highest stress experienced at the ribs. Location measurements presented were taken along the semi-span of the wing from the root and parallel to the aft spar, front spar, and front stringer for each set of sensors.

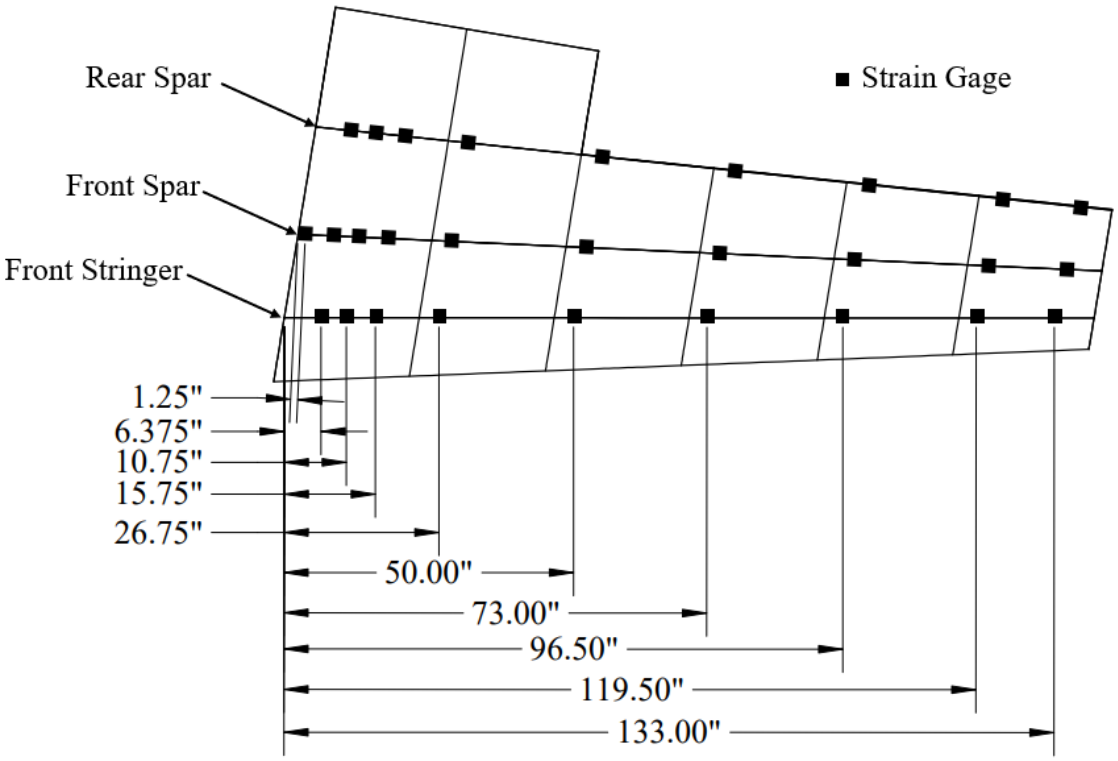

Figure 3.25 Installed Strain Gauge Locations on Upper Skin.

To analyze the stress and displacement experienced by the aircraft wing under the described theoretical loading distribution, multiple sources of data were collected. Regarding theoretical

assumptions for stress, a finite element model was established using Femap NX NASTRAN as a comparison for collected experimental data. The finite model will provide a theoretical source for collected strain data and the overall displacement of the light sport aircraft wing.

During experimentation, strain data will be collected using uniaxial quarter bridge strain gauges adhered along the surface of the wing. While a load is applied to the aircraft wing it is expected that the strain gauges will measure a compressive strain that can be used to determine the compressive bending stress present on the aircraft wing surface. Using the location of the strain gauges, a direct comparison with the finite element model can be established. While it is evident that a properly adhered strain gauge will provide a more accurate stress measurement, the finite element model can indicate strain gauges that may be experiencing significant error. The implemented strain gauges were arranged in a quarter bridge circuit to increase the strain gauges' ability to accurately measure strain in bending.

In addition to applying strain gauges on the wing surface, a strain gauge was applied to the most critical connecting rod to evaluate the load present within the tensile member. This strain gauge will verify the accuracy of the data by providing a percent difference between designed load and actual load applied to the front stringer first rib of the aircraft wing. As failure is most likely to occur at the connection point in which the maximum load is applied, this strain gauge will allow for evaluation of the strength of the connection. One of the strain gauges used during experimentation is presented in Figure 3.26.

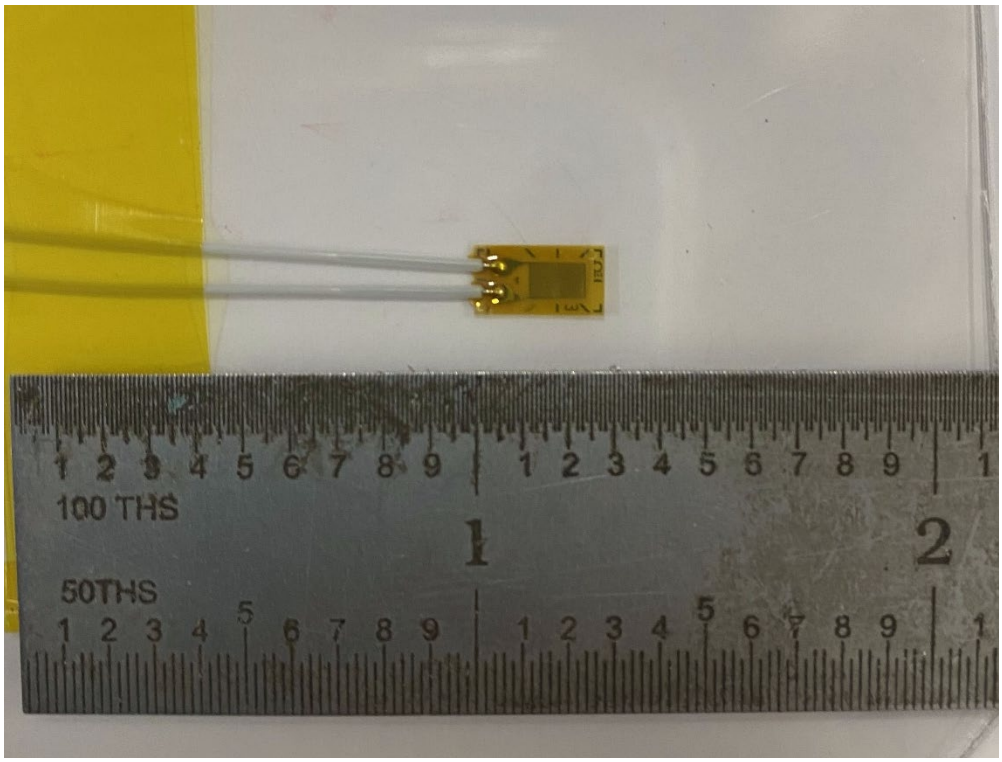

Figure 3.26 Uniaxial Strain Gauge Applied to the Wing Surface.

3.3.2 Data Collection Devices

As strain gauge data is being collected and processed during experimentation, it is clear that a reliable data acquisition system is required. Thus, experts in designing data acquisition systems were consulted during the development of such system. The resultant data acquisition system that was implemented during experimentation is shown in Figure 3.27. Following this system allowed for the facil collection of large datasets to be saved for future analysis using Excel.

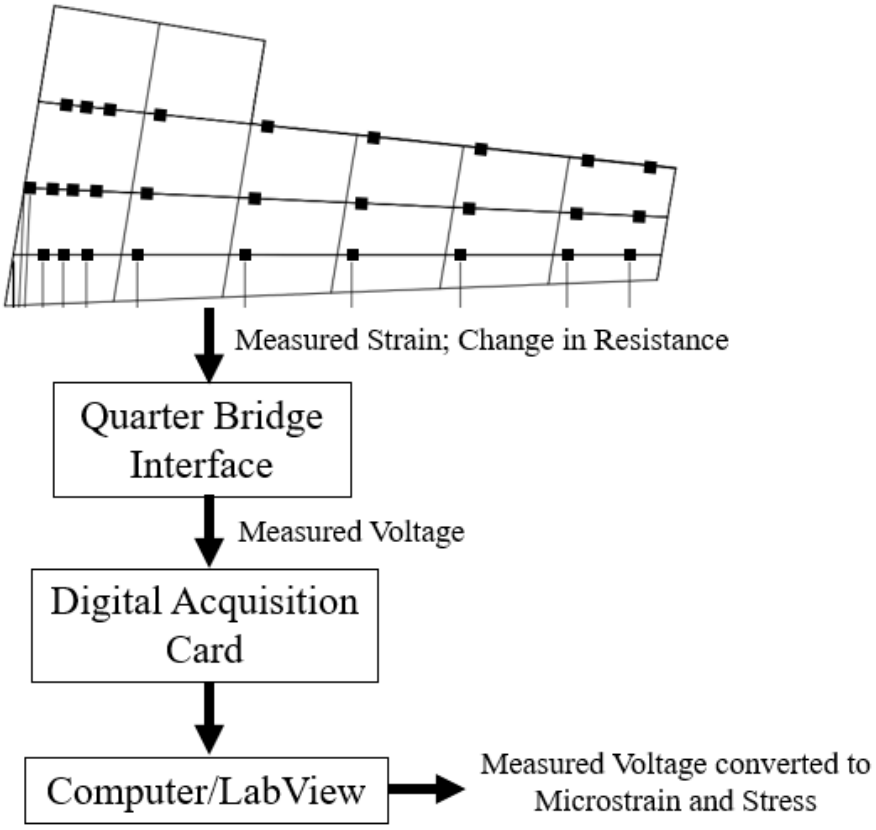

Figure 3.27 Data Acquisition Process.

To ensure strain gauge data was recorded with the highest accuracy possible, a solid-state strain gauge quarter bridge interface was developed specifically for this project. Each strain gauge channel was designed with a potentiometer to ensure that the strain measurements remained in range of the digital acquisition device while strain was being measured. The quarter bridge interface is shown in Figure 3.28. The digital acquisition instrumentation that was utilized to convert the signal from the quarter bridge interface to LabView is described as an NI USB-6218 National Instruments digital acquisition card.

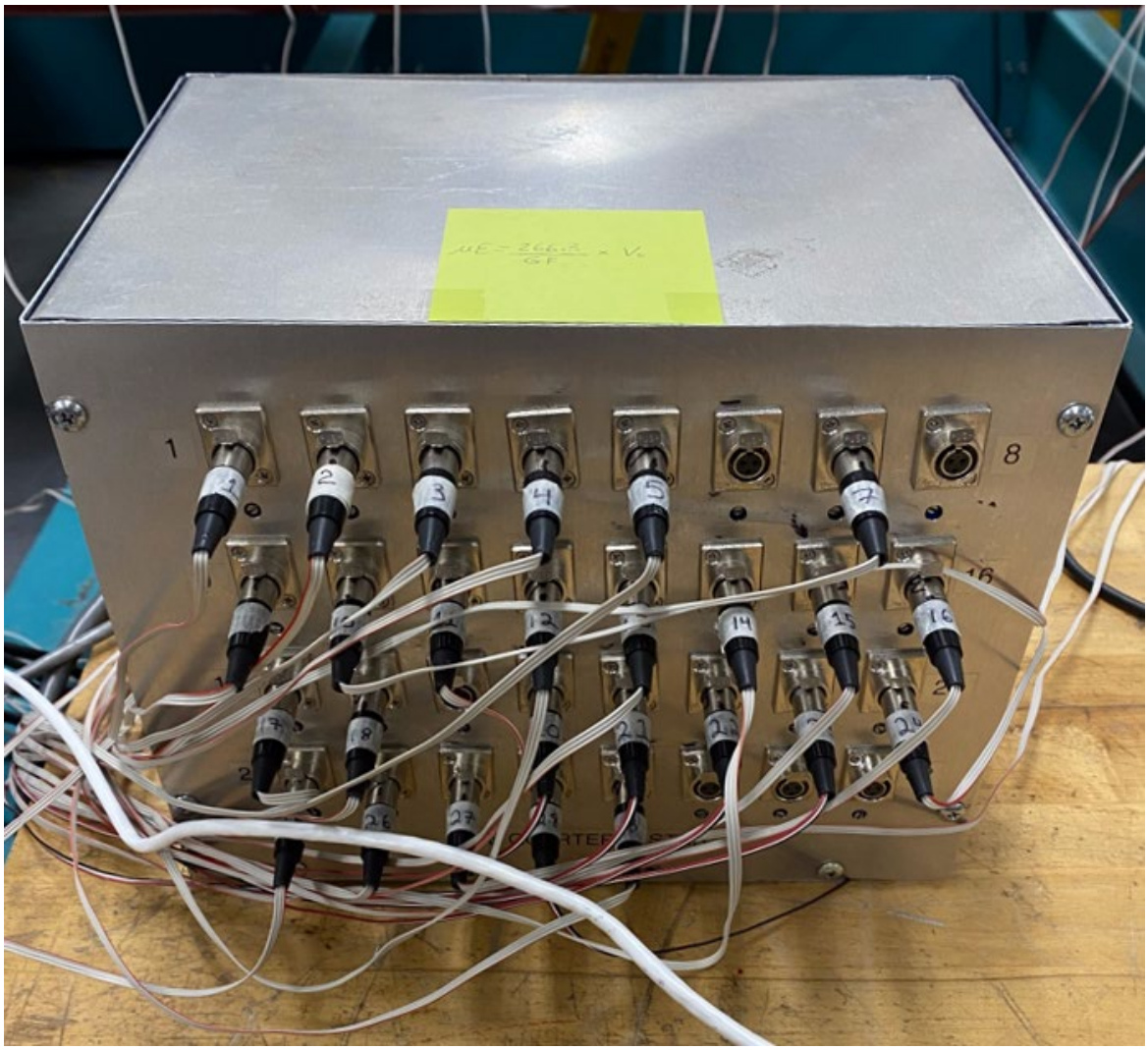

Figure 3.28 Strain Gauge Quarter-Bridge Interface.

To validate the accuracy and precision of the instruments utilized during experimentation, the data collection interface was left powered on to ensure all signals through the system reach a steady state. Prior to performing testing, the aircraft was pre-loaded to 200 pounds and unloaded before taring the system to reduce any residual strain present in the strain gauges. Additionally, multiple tests will be performed to ensure that the strain gauges produced comparable results.

During experimentation, an MTS 407 controller was utilized to control the stroke length of the hydraulic ram responsible for applying the quasi-static load onto the aircraft wing. Atop the

hydraulic ram is a force transducer, shown in Figure 3.29, that is utilized for monitoring the load being applied to the whiffletree structure. Before experimentation, the force transducer is tared after preloading the hydraulic ram to the calculated weight of the whiffletree and wing assembly to ensure no load is being applied to the wing. The overall experimental setup is presented in Figure 3.30.

Figure 3.29 Hydraulic Ram and Force Transducer.

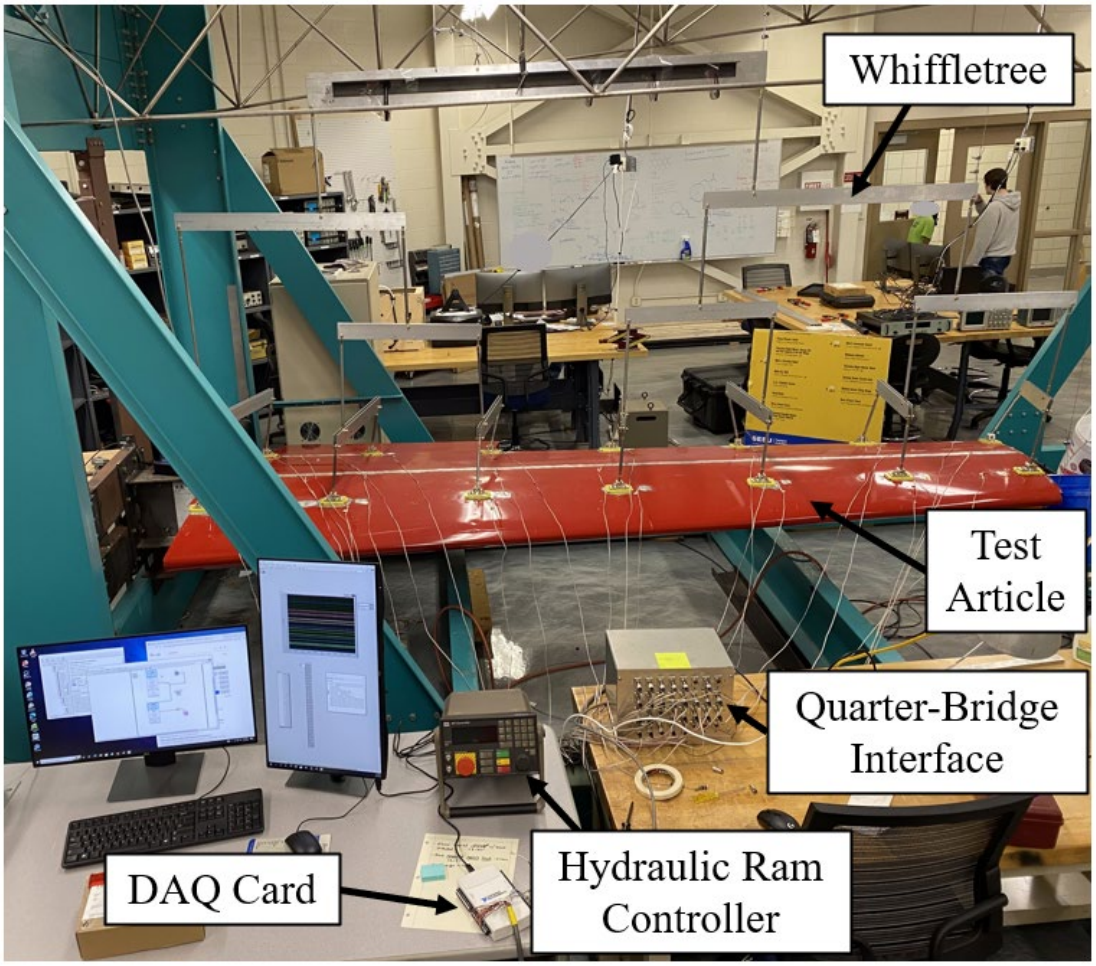

Figure 3.30 Experimental Setup.

4 Results

This section will highlight the relevant results obtained from the finite element model and strain gauges during experimentation applying quasi-static flight loads to the light sport aircraft wing structure. Results in terms of displacement and stress experienced by the wing surface will be discussed. Additionally, the stress experienced by the critical loading connection rod at the front stringer of CWB1 will be analyzed.

4.1 Finite Element Model and Strain Gauges

This section will describe the results obtained from the finite element model and from experimentation applying flight load distribution onto the experimental aircraft. Strain gauge results from previous testing will be included here and a statistical comparison will be made to describe the precision and accuracy of the finite element model. The results from Femap NX NASTRAN for a 660 lb load are presented in Figure 4.1 and Figure 4.2. The results from the finite element analysis are as expected, the highest displacement is experienced at the tip of the wing and the highest stress is experienced towards the root.

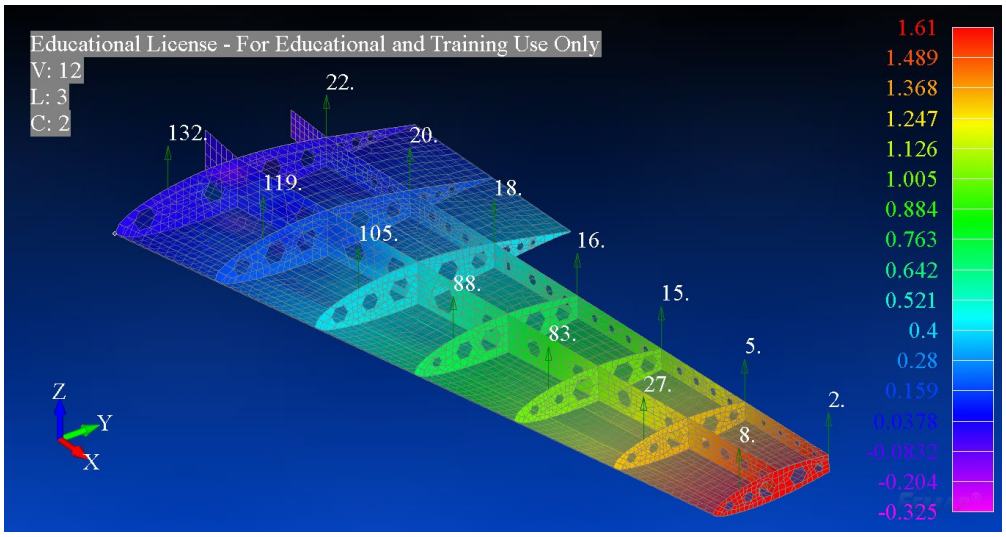

Figure 4.1 Femap NX NASTRAN Light Sport Aircraft Wing Displacement in Inches Under a 660 lb Applied Whiffletree Load.

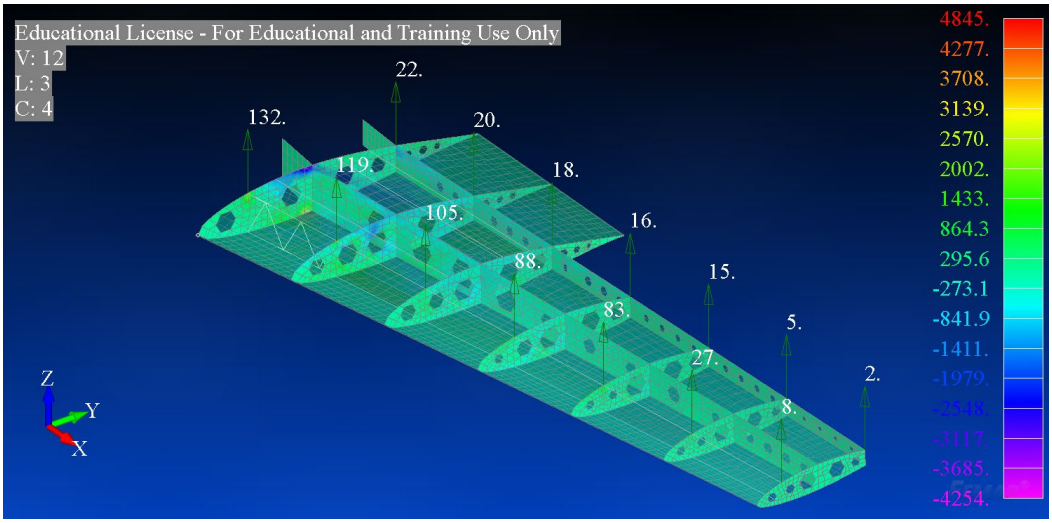

Figure 4.2 Femap NX NASTRAN Light Sport Aircraft Wing Normal X-Direction Stress in Psi Under a 660 lb Applied Whiffletree Load.

Regarding experimentation, three experiments were performed, and the standard deviation of all data sets was taken. The bounds shown on the plots below are two standard deviations from the mean of the collected data. As such, 95 percent of the results from future experimentation is likely to lie within the upper and lower extremes. To improve this statistical model, additional experimentation must be performed.

While performing the first quasi-static wing bending test, noticeable lateral bending occurred in SWB3 after reaching above 500 lbs of load. Due to this bending, testing was halted, and the situation was assessed. To mitigate the bending in SWB3 and eventually SWB2, additional material was added to the beams. Further discussion on this problem will be highlighted later in this report.

Continuing experimentation, failure was experienced in the form of epoxy debonding at the critical rod connection at the front stringer of CWB1 under a load of 570 lbs during experiment 2. After such, it was unclear whether the bonding failure was due to overloading of the wing or due

to the epoxy failing under tension. To analyze this phenomenon, the connection pad was re-adhered to the surface of the wing and an additional strain gauge was installed on the critical loading rod. The goal of this strain gauge was to compare the theoretical load to the actual load acting through the connecting rod. These results are shown, along with their percent differences, in Table 4.1. After applying the designed 660-pound load for the third cycle of experimentation, bonding failure occurred once again, indicating that the failure was not due to overloading but due to the weak tensile strength of the epoxy bond.

Table 4.1 Load on critical connection rod: rib 1, front Stringer

Wing Load (lb)	**Stress (Psi)**	**Theoretical Load (lb)**	**Actual Load (lb)**	**Percent Difference**
0	0	0	0	0
100	1050.27	20	21.22	6.11
200	1421.63	40	40.21	0.52
300	1767.85	60	57.91	3.48
400	2155.12	80	77.71	2.86
500	2545.62	100	97.68	2.32
600	2932.70	120	117.47	2.11
650	3140.68	130	128.10	1.46
660	3175.86	132	129.90	1.59

As no further experimentation could be performed due to lack of materials to properly re-adhere the connection pad, the results from the previous three experiments were analyzed. In regard to displacement, the average displacement experienced by the wing using finite element

analysis was compared to the experimental data. These results are indicated in Table 4.2. From such data, it is evident that there is significant error occurring when lower loading is applied. While not entirely clear, such variation is an indication that there is likely an error with the finite element model as previous testing of the load experienced by the connection rod at the front stringer of rod 1 indicated that the loading experienced by the structure during testing is remarkably close to the designed load.

Table 4.2 Displacement at wing tip

Wing Load (lb)	**Experimental Tip Displacement**	**Femap NX NASTRAN Tip Displacement**	**Percent Difference**
100	0.1458	0.373	60.9
200	0.4166	0.594	29.9
300	0.6666	0.815	18.2
400	0.9583	1.036	7.5
500	1.2708	1.256	1.2
660	1.625	1.61	0.93

The resulting plots comparing the stress experienced along the span of the aircraft wing along the forward spar, aft spar, and front stringer under varying loads are compared to that of the finite element model. These plots are presented on the following pages.

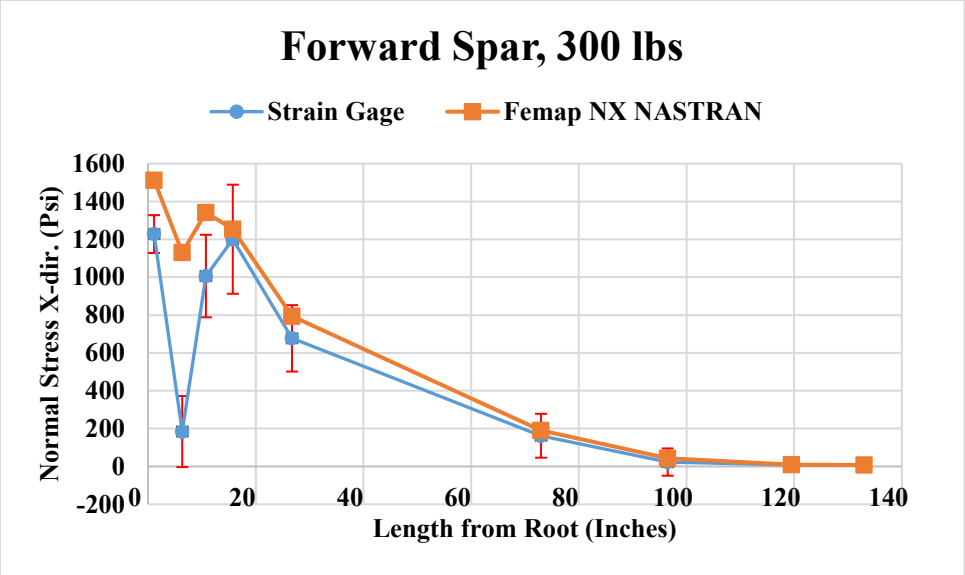

Figure 4.3 Average Strain Gage Stress Measured vs. Finite Element Analysis Results.

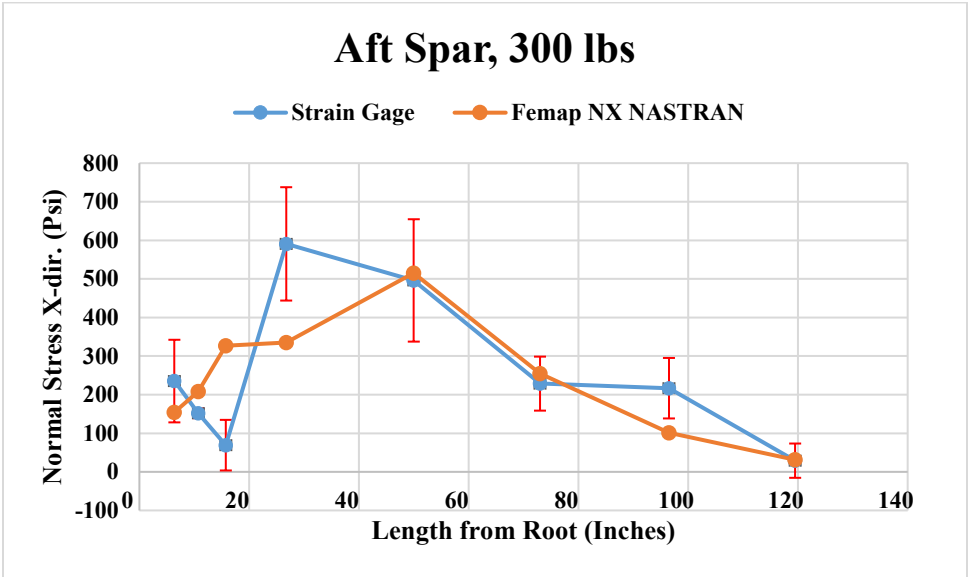

Figure 4.4 Average Strain Gauge Stress Measured vs. Finite Element Analysis Results.

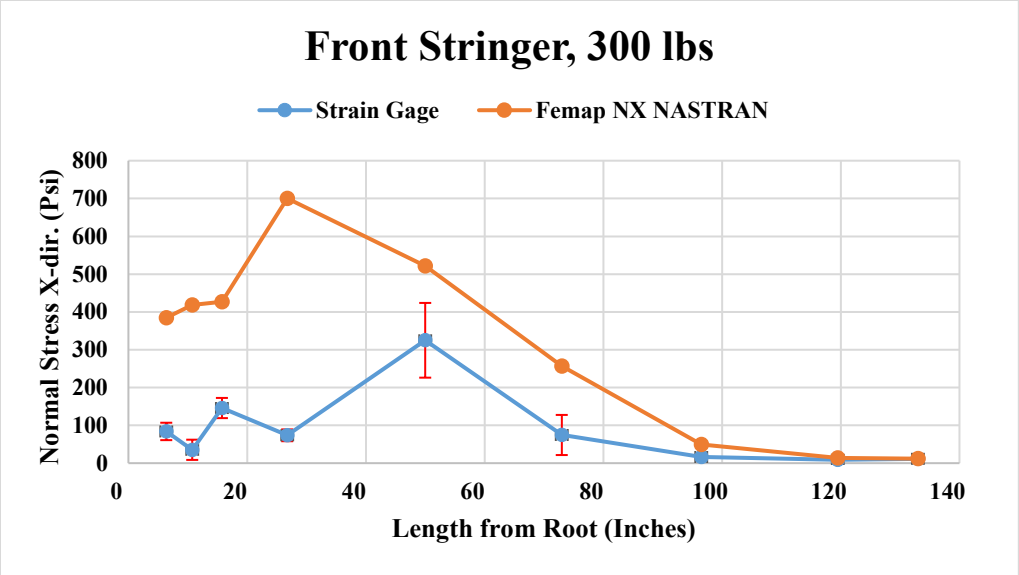

Figure 4.5 Average Strain Gauge Stress Measured vs. Finite Element Analysis Results.

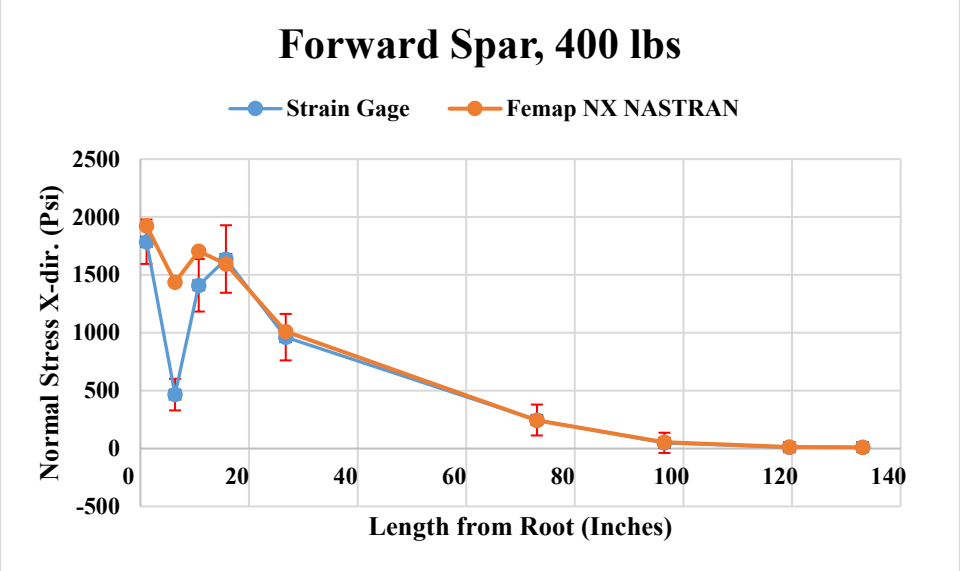

Figure 4.6 Average Strain Gauge Stress Measured vs. Finite Element Analysis Results.

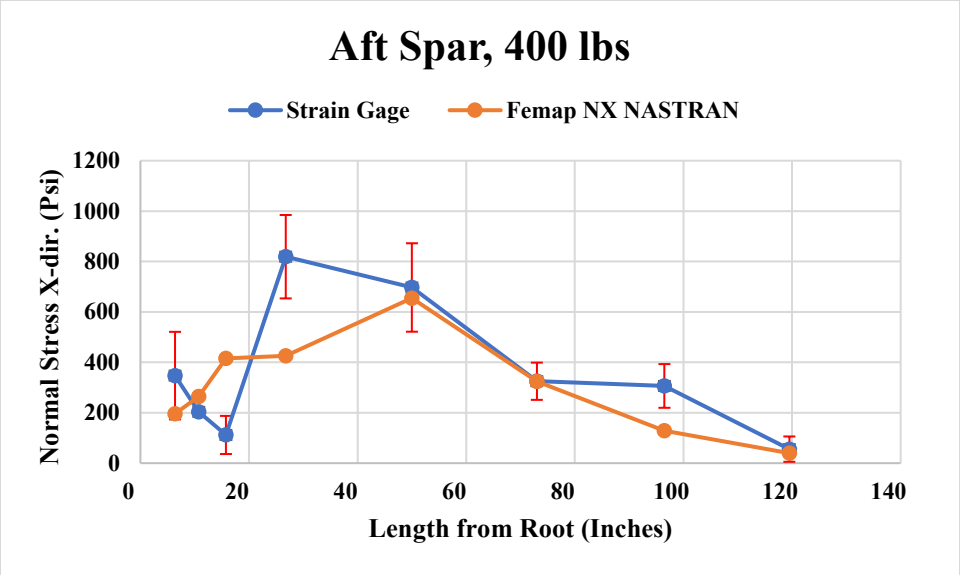

Figure 4.7 Average Strain Gauge Stress Measured vs. Finite Element Analysis Results.

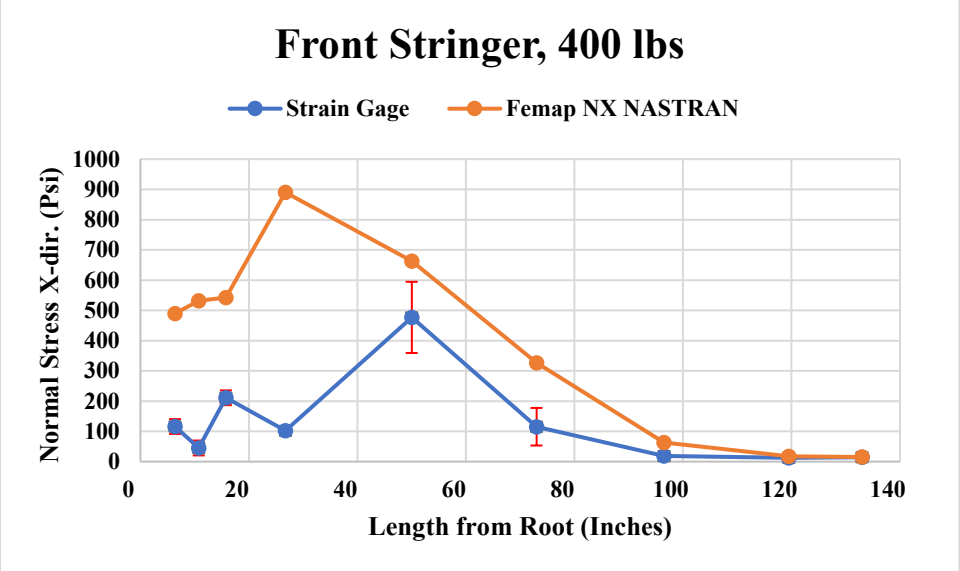

Figure 4.8 Average Strain Gauge Stress Measured vs. Finite Element Analysis Results.

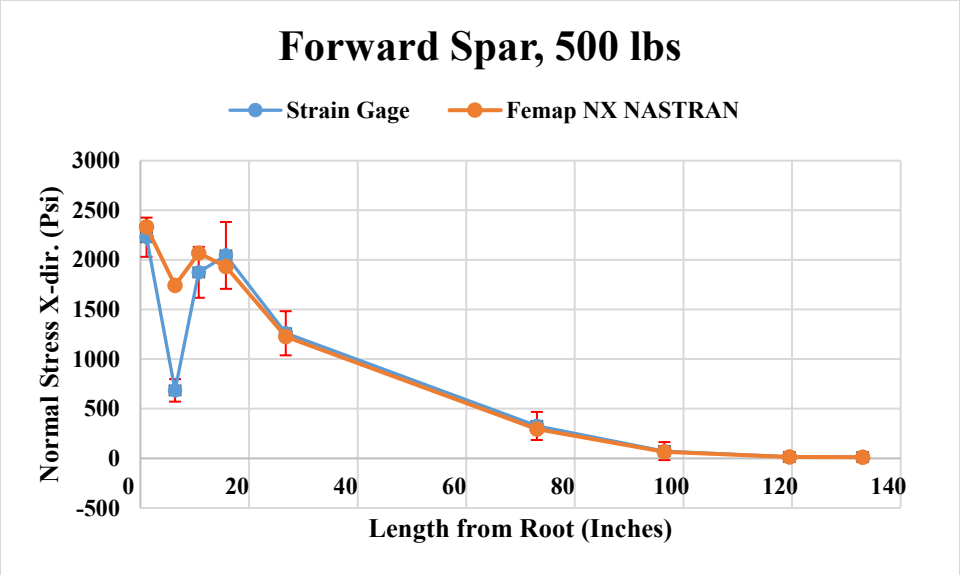

Figure 4.9 Average Strain Gauge Stress Measured vs. Finite Element Analysis Results.

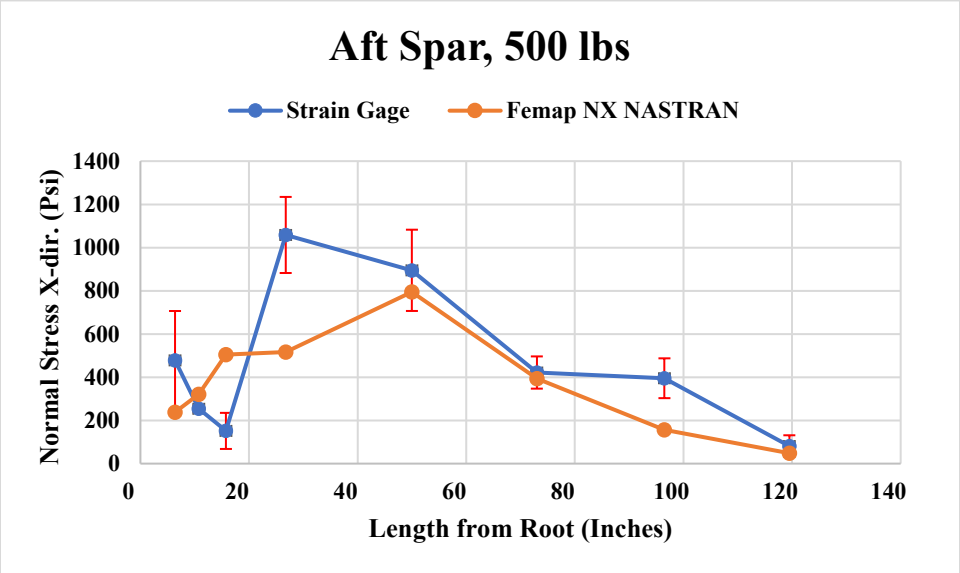

Figure 4.10 Average Strain Gauge Stress Measured vs. Finite Element Analysis Results.

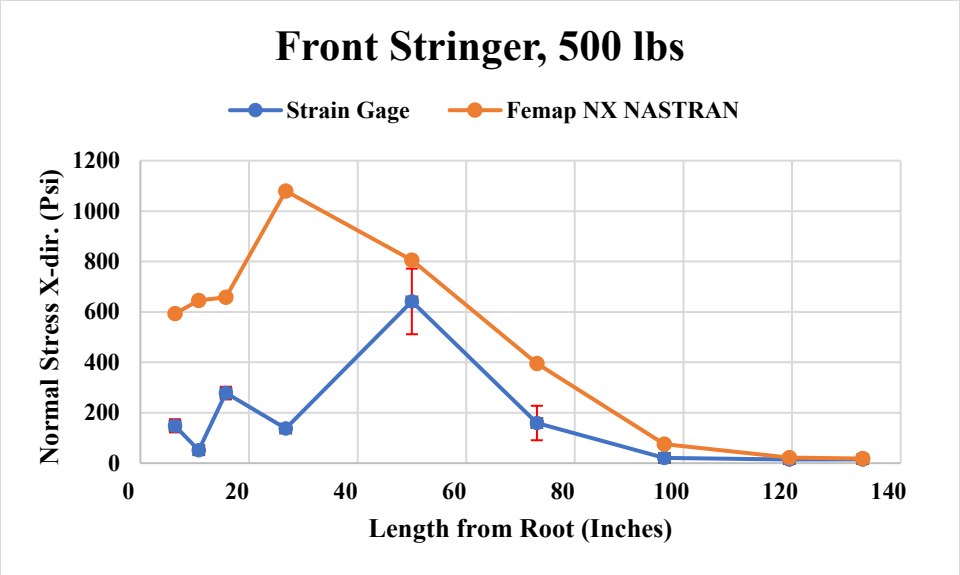

Figure 4.11 Average Strain Gauge Stress Measured vs. Finite Element Analysis Results.

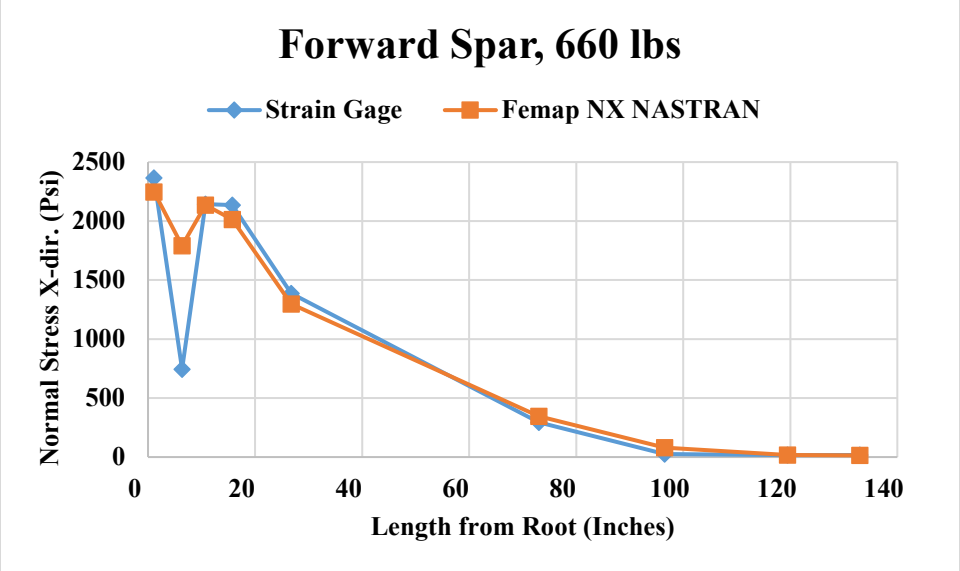

Figure 4.12 Average Strain Gauge Stress Measured vs. Finite Element Analysis Results at 1G Load.

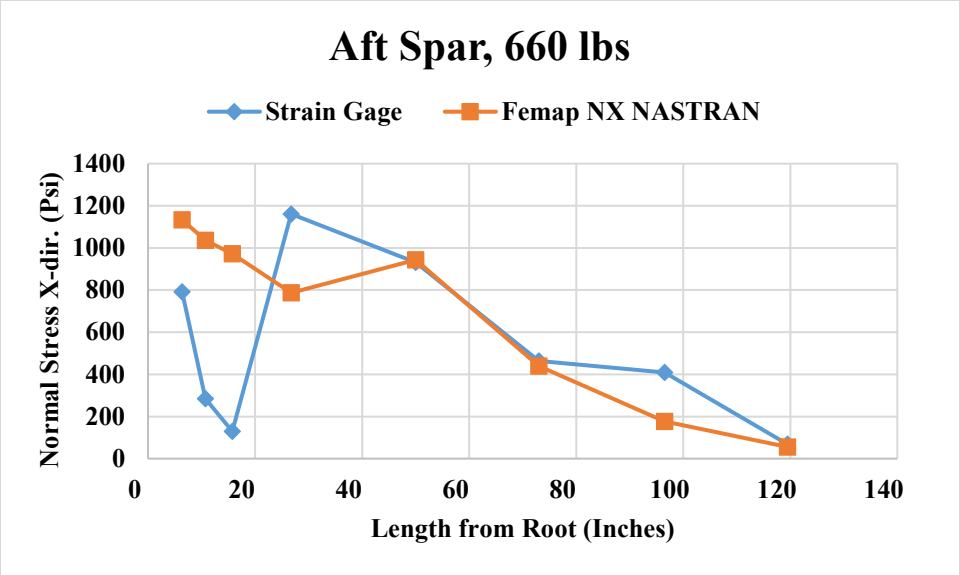

Figure 4.13 Average Strain Gauge Stress Measured vs. Finite Element Analysis Results at 1G Load.

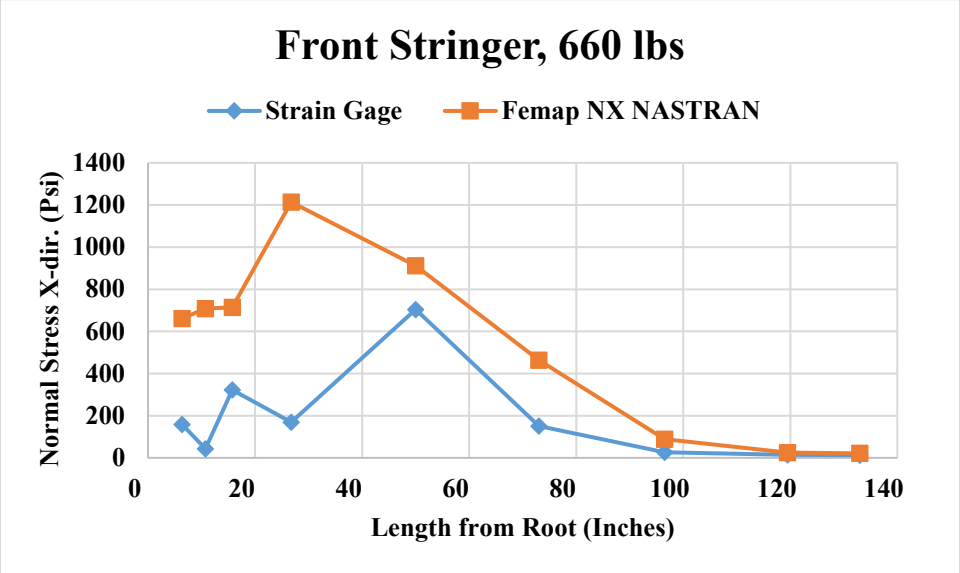

Figure 4.14 Average Strain Gauge Stress Measured vs. Finite Element Analysis Results at 1G Load.

5 Discussions, Conclusions, and Recommendations

This section will discuss the results from the finite element model and strain gauge data. Additionally, this section will provide insight into sources of experimental error and recommended further enhancements to increase the accuracy of the developed model.

5.1 Discussion

Some of the results obtained in the previous section were not hypothesized, but were not entirely unexpected, as it is difficult to model complex structures and assemble experiments to represent reality. Beginning with the most plausible result, the load acting on the wing structure was analyzed through the load acting upon the front stringer of CWB1. When comparing this load to the theoretical designed load, the average percent difference including all loading cases is 2.5 percent. Thus, indicating the actual load applied to the wing structure is most likely very close to the designed load. Further experimentation and analysis of additional rod structures must be completed to determine this statement conclusively.

Analyzing the displacement results, it is evident that there is likely an inaccuracy involved in the development of the finite element model. Under the assumption that the whiffletree load is close to the designed load using the limited data collected, it is evident that the finite element model is not an accurate representation of the structure considering the displacement data. This discontinuity is likely a result of the idealized stringers and flanges used in the development of the finite element structure as the idealized elements are assumed to be rods with a specified area. In the actual wing structure these elements are angled plates which are more resistant to bending loads. It is also important to consider the error present during low load cases caused by the weight of the whiffletree structure which may have an effect on the load distribution and wing deflection.

Evaluating the results of the stress distribution along the wing compared to the finite element model, there are additional discontinuities that support the previous statement regarding he

idealized stringers. From these results, it is indicated that the stress experienced by the forward spar and front stringer are relatively accurate in comparison to the finite element model. The variation in compressive stress experienced for the forward spar and front stringer is noticed in the first section of the wing. Alas, this difference in stress is likely due to the additional shear plate adhered to the web of the forward spar in the first bay on the actual model that is not existent in the finite element model. This additional stiffness may also explain why the stress experienced in wing bay closest to the root is decreasing from the root but increases again after the next rib structure. Another consideration in the variation in measured normal stress may be due to the slight outward deformation of the skin in the wing bay that is prevalent during bending.

Considering the results from the aft spar, no definitive conclusions can be drawn between the finite model and the measured stress. Regarding the variation present between the different tests, it is evident that the wing or strain gages may be experiencing residual strain from previous testing or due to temperature variation throughout the testing period. For future testing this large variation in measured strain must be addressed. As the accuracy of the model is restricted due to the failure of the bond at the primary connecting pad, no additional conclusions can be drawn relative to the collected data at this time.

During preliminary experimentation, it was evident that there were multiple significant problems with the design of the whiffletree structure. These design mishaps were extended through the previous development of the whiffletree structure that was inherited and reanalyzed for the described experimentation. The First primary difficulty facing the wing structure was that the moment arm due to the weight of the material was not accounted for during load analysis. As such, the applied load to the whiffletree structure was not as intended as the load distribution is highly dependent on the force variation due to the moment arms. This variation in loading is more evident

during lower loading steps as the whiffletree is unable to counter the weight of the structure leaving some ribs with no applied loads.

To mitigate this issue, a ballast, or counterweight, was designed for each beam to counter the undesigned moment arm. These calculations were completed by assuming static equilibrium and equating the sum of the moments acting about the center hole of each beam as zero. During such design, it was important to evaluate the moments starting at the chordwise beams as the counterweights provided an additional moment arm to the spreader beams acting above. After completing these calculations, it was evident that the weight required to counter the moment arm about SWB1 and SWB3 was too large due to the large variations in moment arms. To mitigate this issue, a pulley system was designed to instead apply a significantly smaller upwards load on the larger moment arm of the spreader beams. The required counterweights calculated are presented in Table 5.1 and Table 5.2.

Table 5.1 Spanwise counterweight loads and direction of applied loads.

Beam (lb)	**Counterweight Required (lb)**	**Load Direction**
SWB1	8.324	Upwards
SWB2	0.985	Downwards
SWB3	20.948	Upwards
SWB4	0.422	Downwards
SWB5	0.098	Downwards
SWB6	7.434	Downwards

Table 5.2 Chordwise counterweight loads and direction of applied loads.

Beam (lb)	**Counterweight Required (lb)**	**Load Direction**
CWB1	7.218	Downwards
CWB2	6.902	Downwards
CWB3	6.629	Downwards
CWB4	5.553	Downwards
CWB5	5.211	Downwards
CWB6	4.505	Downwards
CWB7	4.326	Downwards

To put these values into perspective, relative to the moment arm lengths, SWB3 required a 130 lb downwards counterweight along the short moment arm or a 20 lb upward pulley counterweight on the long moment arm. Considering such, an upward pulley was designed to mitigate the unbalance of moments in SWB3. A demonstration of the whiffletree with the designed counterweights is shown in Figure 5.1.

Figure 5.1 Light Sport Aircraft Wing with Counterweights.

While not an ideal solution, the designed counterweights were successful in eliminating the imbalance of moment arms. Although a significant quantity of mass was added to the structure, such mass can be mitigated by increasing the tare load on the testing structure.

The second difficulty that faced the whiffletree structure existed in the spreader beams. While each beam was designed to resist bending and buckling in the loading direction, this analysis assumed that the load will be applied along one vertical plane passing through the beam centroid.

In practice, this assumption does not stand true. As the whiffletree is designed to be flexible and the tree structure is designed to change shape during bending, the loads experienced by the beams were not ideal. As such, significant lateral bending occurred when applying loads greater than 300 lbs, halting experimentation to prevent catastrophic failure.

While initially, lateral bending was only occurring on the critical SWB1, as the load exceeded 500 lbs significant bending occurred in SWB2 and SWB3. To mitigate bending in SWB1 a steel angle beam was clamped to the structure. After such, the first set of data was collected until SWB2 and SWB3 experienced lateral bending as well. Once this occurred, experimentation was halted, and the situation was evaluated. The demonstrated issue was evidently a problem associated with the cross section of the spreader beams not being resistant to the lateral bending. To mitigate this issue, additional channel beams were developed using 1/8-inch aluminum plates and aluminum angle bars. These beams were adhered directly to SWB2 and SWB3, as shown in Figure 5.2, to create a cross section similar to a channel beam. This solution was effective in mitigating the lateral bending in SWB2 and SWB3 during experimental loading.

Figure 5.2 Channel Section Adhered to SWB2.

Another issue that arose during experimentation was the failure of the bond at the critical loading point, the front stringer of rib 1. Initial bonding failure occurred at 630 lbs while collecting the second set of data. Once failure occurred, the test was aborted, and damage was assessed. From such assessment, it was evident that the epoxy bonding failed at the rivet heads. While uncertain whether failure was solely due to the uneven bonding layer, the residual epoxy was removed from the aircraft wing and connection pad. After such, the surface was prepped and re-bonded, similar to the experimental test model used to check the effectiveness of the adhesive, and testing was continued. While performing a third test, the bond once again failed at an applied whiffletree load of 729 lbs. The failed bonding surfaces are shown in Figure 5.3 and Figure 5.4.

Figure 5.3 CWB1 Bonding Failure Connecting Pad.

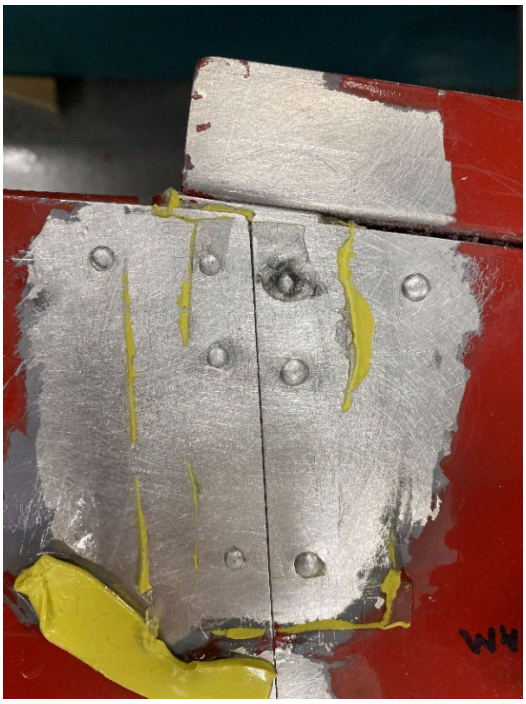

Figure 5.4 CWB1 Bonding Failure Wing Surface.

Analyzing these cross sections, it is evident that failure occurred at the rivet heads, indicating that the utilized epoxy does not have sufficient adhesion for a varying bond line. This problem must be mitigated for any future experimentation to be performed successfully.

5.2 Conclusions

From the described experimentation, it is evident that the strain gages and developed finite element model are precise and accurate at measuring and predicting the uniaxial strain present along the forward spar and front stringer of the experimental aircraft structure for each loading phase. All measured strain values for the forward spar at each loading phase were within two standard deviations of the mean. Variation experienced in the first wing bay between ribs 1 and 2 is likely due to the addition structure added inside the wing to prevent shear buckling that is not modeled on the finite element model. While peculiar that the strain gages between the ribs experience a reduced stress, this phenomenon is likely due to the increased stiffness in the wing bay closest to the root and may also be affected by the very small outward bowing of the skin

between the ribs during loading. Considering the simplifications in the finite element model causing potential inaccuracies in the model, it is evident that the properly adhered strain gages demonstrate a more accurate representation of the stress acting about the wing surface.

Regarding the geometry utilized to develop the presented model, it is evident that a modified two beam whiffletree structure, such as that presented in this paper, can be successfully implemented to apply distributed flight loads to an aircraft wing structure. It is also conclusive that the load experienced in the most critical connecting rod at the front stringer of CWB1 is very close to the designed load. While the assumption can be made that this is an indication the whiffletree is distributing the designed load distribution, additional strain gauges need to be utilized on other connecting rods to make this statement decisive.

5.3 Recommendations

Regarding future experimentation, it is evident that some changes should be made to the design of the overall whiffletree structure. As the chosen cross section was inadequate for preventing lateral bending, it is suggested that the spreader beams be redesigned using channel beams assembled web to web with the spherical bearing heads between the web sections. Alternative cross sections that resist both longitudinal and lateral bending and buckling are also recommended, including box cross sections.

Additionally, rather than arbitrarily choosing a beam size and analyzing the experienced loads acting upon the member, it is recommended to determine the section properties required to resist the maximum moments, including the design margin of safeties, and compare the calculated section properties to that of the decided cross section at varying sizes. After choosing a sufficient cross section size, additional analysis can be easily performed to evaluate worst case scenario loading similar to which was completed in this report.

Furthermore, when designing the whiffletree spreader beams, it is important to consider the effect that gravity will have on the moment arm of the beam. Such moment arm difficulties can be eliminated by countering out the moment due to gravity acting on the beams by including additional beam material on the end with the short moment arm. It is also important to consider the weight acting on each spreader beam from the spreader beams below as these masses can significantly affect the moment arm.

To ensure the chordwise load is as accurate as possible, changing the position in which the spanwise whiffletree plane connects to the chordwise beams may result in a more accurate chordwise distribution. While the model presented is sufficient in terms of loading the ribs to proper loads, the torsional loads experienced by the wings may not be completely accurate as the relationship between the load acting at the front and aft of the wing is not perfectly represented of the chordwise pressure distribution as the aerodynamic coupling is not represented. This coupling will introduce a leading edge down torsional moment. Changing the connection points on the chordwise beams to consider this aerodynamic pitching moment will mitigate this inaccuracy.

It is also recommended that the epoxy bonding the footpad be reassessed. Ensuring the bonding agent is produced specifically for bonding metal to metal rather than as a composite matrix material. A potential candidate for bonding the connecting pad to the wing surface is Loctite EA 9330 Aero. This bonding paste has sufficient material properties and maintains good bonding even with varying bond line thickness. Alternative metal to metal bonding epoxy or paste may also be sufficient for this application. Additional consideration for creating a bracket to encase the rib structure rather than relying on point load should be considered. Utilizing a bracket structure will allow for an increased load to be applied to the wing without the risk of bond failure. It is important to note that to apply loading greater than 1G, an alternative whiffletree must be designed.

Regarding the accuracy of the finite element model utilized during experimentation, much improvement can be made to increase the fidelity of the model. Particularly, additional plate elements were added onto the wing model after initial design to prevent shear buckling; this is not present in the current model. Also, the stringers and flanges are currently modeled as idealized structures rather than their actual geometries. These model simplifications can have a significant effect on the model that must be addressed in future testing. Additionally, the plate elements utilized to construct the model were all modeled for experiencing bending loading while they are designed for experiencing shear and thus should be modeled as shear panels.

In closing, while the results of this report were unsuccessful in the development and implementation of a high-fidelity finite element analysis and experimental model, a plethora of recommendations for future experimentation are established. The analysis presented in this report demonstrates a fundamental basis for the development of a whiffletree model for use on future aircraft quasi-static analysis structures.

6 REFERENCES

[1] Hoversten, P. Then & Now: Under Stress. Smithsonian Magazine, Apr, 2009.

[2] Taylor, R. M., Lira, N., Sabine, G., Lea, J., Conklin, C., Niakan, B., and Advirkar, S. "Design Optimization, Fabrication, and Testing of a 3d Printed Aircraft Structure Using Fused Deposition Modeling." *AIAA Scitech 2020 Forum*, Vol. 1 Part F, No. January, 2020, pp. 1–16. https://doi.org/10.2514/6.2020-1924.

[3] Chinvorarat, S., Watjatrakul, B., Nimdum, P., Sangpet, T., Soontornpasatch, T., and Vallikul, P. "Static Testing for Composite Wing of a Two-Seater Seaplane." *IOP Conference Series: Materials Science and Engineering*, Vol. 501, No. 1, 2019. https://doi.org/10.1088/1757-899X/501/1/012026.

[4] Roessler, C., Stahl, P., Sendner, F., Hermanutz, A., Koeberle, S. J., Bartasevicius, J., Rozov, V., Breitsamter, C., Hornung, M., Meddaikar, Y. M., Dillinger, J. K. S., Sodja, J., de Breuker, R., Koimtzoglou, C., Kotinis, D., and Georgopoulos, P. "Aircraft Design and Testing of Flexop Unmanned Flying Demonstrator to Test Load Alleviation and Flutter Suppression of High Aspect Ratio Flexible Wings." *AIAA Scitech 2019 Forum*, No. January, 2019, pp. 1–20. https://doi.org/10.2514/6.2019-1813.

[5] Miller, E. J., Li, W., Jordan, A., and Lung, S. F. "X-57 Wing Structural Load Testing." *Aiaa Aviation 2020 Forum*, Vol. 1 PartF, 2020, pp. 1–19. https://doi.org/10.2514/6.2020-3090.

[6] Horizon Light Sport Aircraft. *Light Sport Aircraft Pilot News Magazine*. http://www.lightsportaircraftpilot.com/horizon_experimental_lightsportaircraft/index.html%0A.

[7] Abbott, I., and Von Doenhoff, A. *Theory of Wing Sections*. New York, 1949.

[8] Septiyana, A., Rizaldi, A., Hidayat, K., and Wijaya, Y. G. "Comparative Study of Wing Lift Distribution Analysis Using Numerical Method." *Jurnal Teknologi Dirgantara*, Vol. 18, No. 2, 2020, p. 129. https://doi.org/10.30536/j.jtd.2020.v18.a3349.

[9] Gudmundsson, S. *General Aviation Aircraft Design: Applied Methods and Procedures*. Elsevier Incorporated, 2014.

[10] Silitonga, F. Y., and Moelyadi, M. A. "Comparative Study of Wing Lift Distribution Analysis for High Altitude Long Endurance (HALE) Unmaned Aerial Vehicle." *Journal of Physics: Conference Series*, Vol. 1005, No. 1, 2018. https://doi.org/10.1088/1742-6596/1005/1/012036.

[11] Prandtl, L. *Applications of Modern Hydrodynamics to Aeronautics*. 1923.

[12] Anderson, J. D. *Fundamentals of Aerodynamics (6th Edition)*. 2011.

[13] Cook, M. V. *Flight Dynamics Principles*. 2007.

[14] Glauert, H. *The Elements of Aerofoil and Airscrew THeory*. Cambridge University Press, London, 1926.

[15] Lizotte, A. M., and Lokos, W. A. "Deflection-Based Structural Loads Estimation From the Active Aeroelastic Wing F / A-18 Aircraft." No. May, 2005.

[16] Lizotte, A. M., and Lokos, W. A. "Deflection-Based Aircraft Structural Loads Estimation with Comparison to Flight." *Collection of Technical Papers - AIAA/ASME/ASCE/AHS/ASC Structures, Structural Dynamics and Materials Conference*, Vol. 4, 2005, pp. 2698–2715. https://doi.org/10.2514/6.2005-2016.

[17] Lokos, W., Eric, M., Hudson, L., Holguin, A., Neufeld, D., and Haraguchi, R. "Strain Gage Loads Calibration Testing With Airbag Support for the Gulfstream III Subsonic

Research Aircraft Testbed." *AIAA Science and Technology Forum*, 2015.
[18] Molent, L. "The History of Structural Fatigue Testing at Fishermans Bend Australia."
[19] Ula, N. M., Marta, A., Wijaya, Y. G., and Muksin. "Wing Static Test of LSU-02 NGLD Aircraft Using Whiffletree Method." *AIP Conference Proceedings*, Vol. 2088, No. April, 2019. https://doi.org/10.1063/1.5095330.
[20] Warsi Sullivan, R., Hwang, Y., Rais-Rohani, M., and Lacy, T. "Structural Analysis and Testing of an Ultralight Unmanned-Aerial-Vehicle Carbon-Composite Wing." *Journal of Aircraft*, Vol. 46, No. 3, 2009, pp. 814–820. https://doi.org/10.2514/1.36415.
[21] Ma, S. F., and Shiue, T. K. "Aircraft Airworthiness Certification: Static Bench Testing of an Airfoil Elevator." *Experimental Techniques*, Vol. 27, No. 1, 2003, pp. 32–35. https://doi.org/10.1111/j.1747-1567.2003.tb00097.x.
[22] Yeniceli, S. C. "Design Optimization of Whiffletree Systems for Wind Turbine." No. January, 2014, p. 123.
[23] Shapira, O., Simon, U. B., Glam, B., Bergman, A., Rothman, T., Haris, E., Kressel, I., and Tur, M. "Structural Integrity Monitoring of Composites-Based Uav Wings Using Fiber Optic Distributed Strain Sensing." *55th Israel Annual Conference on Aerospace Sciences 2015*, Vol. 1, No. February, 2015, pp. 113–116. https://doi.org/10.13140/RG.2.1.3943.2808.
[24] Jutte, C. V., Wieseman, C. D., Lovejoy, A. E., and Stanford, B. K. "Static Loads Testing of a High Aspect Ratio Tow-Steered Wingbox." *AIAA Scitech 2020 Forum*, Vol. 1 Part F, 2020, pp. 1–21. https://doi.org/10.2514/6.2020-0243.
[25] Lovejoy, A. E., Gardner, N. W., Dawicke, D. S., Jutte, C. V., and Smith, B. "Improving Structural Test and Analysis Correlation Using Digital Image Correlation Boundary Measurements." *AIAA Scitech 2020 Forum*, Vol. 1 PartF, No. January, 2020, pp. 1–18. https://doi.org/10.2514/6.2020-2188.
[26] Martin, J. *Engineering Report No. ER-X-01-0001 Prototype Design Loads Model Number 01*. 2009.
[27] Patel, D. *Red Wing Project*. 2019.
[28] *METALLIC MATERIALS AND ELEMENTS FOR AEROSPACE VEHICLE STRUCTURES*. Department of Defense, 2003.
[29] *Steel Construction Manual*. American Institute of Steel Construction, 2011.
[30] Industries, S. W. TRAK K3 CNC Knee Mills. https://www.southwesternindustries.com/products/knee-mills.
[31] NASA. *NASA-TM-X-73305 Astronautic Structures Manual*. 1975.